A Hybrid Quantum-Classical Simulation Study on the Li Diffusion in Li-Graphite Intercalation Compounds

(Li-グラファイト層間化合物中のLi拡散に関する
ハイブリッド量子古典シミュレーション)

by
Nobuko Ohba

Submitted to
the Department of Scientific and Engineering Simulation
in partial fulfillment of the requirements for the degree of
Doctor of Engineering
at
Nagoya Institute of Technology

2012

Abstract

The challenges in high usage of renewable energy resources such as the solar power, wind power, and biomass fuel have been addressed recently in both academic and commercial societies to solve the global warming and fossil fuel exhaustion problems. Under the situation, automakers have accelerated the development and practical applications of green vehicles or environmentally friendly vehicles as hybrid cars, plug-in hybrids, electric cars, and fuel cell-powered hydrogen cars. Rechargeable batteries are indispensable for these green vehicles, and the research and development have focused on the lithium (Li) ion rechargeable battery because of its high energy density. In the battery, the Li ions are shuttled between the positive and negative electrodes by the applied voltage through the nonaqueous electrolyte and separator. Such charge and discharge reactions in the Li-ion battery involve following key processes: the transport of the Li ions in both electrode and electrolyte materials, the charge transfer at the electrolyte-electrode interfaces, and the internal structural changes of the electrodes relating to the increase in the Li density. Much interest exists to advance the power, capacity, recharging speed, and durability of the Li-ion battery.

The graphite can form various intercalation compounds by incorporating atoms (ions) and small molecules between the carbon (C) layers. Among these, the Li-graphite intercalation compound (Li-GIC) is put to practical use as a negative electrode of the Li-ion rechargeable battery. Among the key processes, the transport process of the Li ions in the graphite layers is related directly to the power performance of the Li-ion batteries. In the Li insertion process of the Li-GIC, the Li ion creates a long-ranged stress field around itself by expanding the inter-layer distance of the graphite. To take into account such a long-ranged stress field in the first-principles simulation of the Li diffusion, the hybrid quantum (QM)-classical (CL) simulation code is developed. In the hybrid code, the QM region selected adaptively around the Li ion following its motion is treated with the real-space density-functional theory. The rest of the total system is described with an empirical interatomic potential that includes a novel formula for the dispersion force between the C atoms that belong to different layers. Buffered cluster method is applied

for coupling of the QM and CL regions.

In the present thesis we firstly perform a series of the hybrid QM-CL simulation runs for the dynamics of a single Li-ion in the graphite at temperature of 423 K for various values of the averaged inter-layer distance. It is found that the Li diffusivity is suppressed substantially when the inter-layer distance is compressed by a few percent from the equilibrium value. On the other hand, the Li diffusivity is unaffected by the stretching of the inter-layer distance up to a few percent. In the equilibrium and stretched cases, the diffusive motion of the Li ion is composed of ballistic and hopping modes. In the compressed case, the Li ion diffuses in the hopping mode only and is confined in a small area at long times. Separately the activation energy for the hopping diffusion is calculated at zero temperature to find that it is as small as 0.1 eV and that the substantial contribution comes from the deformation energy of the whole system. Based on the findings we propose a novel mechanism to explain the unique Li-density dependence of the Li diffusivity observed experimentally in the Li-GIC.

We secondary analyze the relation between the vertical position and diffusivity of the Li ion in graphite. The Li diffusivity is enhanced when the Li ion escapes from one of the two stable vertical sites to move around the middle of the upper and lower C-layers where a resisting force on the Li ion for the perpendicular motion is relatively weak.

Considering the analyses, we thirdly perform additional hybrid simulation runs for the Li dynamics in graphite at 423 K under various settings of the amplitude and frequency of alternating electric fields perpendicular to C-layers. The in-plane diffusivity of the Li ion is enhanced significantly by the electric field if the amplitude is larger than 0.2V/Å within its order and the frequency is as high as 1.7 THz. The microscopic mechanisms of the enhancement are explained.

Contents

1 Introduction **1**

1.1 Motivation 1

1.2 MD for CL dynamics calculation 4

1.2.1 Molecular dynamics 4

1.2.2 Time integration of equation of motion 6

1.3 Density functional theory for QM calculation 6

1.3.1 Basis of theory 6

1.3.2 Kohn-Sham equation 9

1.3.3 Real space implementation 12

1.4 Hybrid quantum classical simulation 15

1.4.1 Buffered cluster method 15

2 Application for carbons **19**

2.1 Settings in CL calculation 19

2.1.1 Brenner-type potential for intra-layer of carbons 19

2.1.2 Derivatives of Brenner-type potential 22

2.1.3 Model potential for inter-layer of carbons 24

2.2 Results and Discussion 27

2.2.1 Validity of intra-layer potential model of carbons . . . 27

2.2.2 Validity of inter-layer potential model of graphite . . . 27

3 Preparatory calculations **31**

3.1 Hybrid QM-CL simulation of diamond 31

3.2 Hybrid QM-CL simulation of graphite 32

3.3 Hybrid QM-CL simulation of Li-GIC 33

4 Stress-dependence of Li diffusivity in graphite **41**
4.1 Introduction 41
4.2 Hybrid QM-CL simulation method 43
4.2.1 Buffered cluster method 44
4.2.2 QM calculation 44
4.2.3 CL calculation 45
4.2.4 Target system 46
4.3 Results and discussion 48
4.4 Conclusions 61

5 Enhanced thermal diffusion of Li in graphite by alternating vertical electric field **63**
5.1 Introduction 63
5.2 Settings in simulation 65
5.3 Results and discussion 69
5.4 Conclusions 72

6 Summary **75**

Acknowledgments **79**

References **81**

List of Tables

2.1 Parameters of Brenner-type potential. 21
2.2 Physical properties of diamond and graphite obtained from the CL-MD calculation with the Brenner-type potential. . . . 28
2.3 Properties related to inter-layer interaction of graphite. . . . 29

4.1 The results of various quantities at the ground state (GS) and transition state (TS) calculated using the VASP code. The $E_{\rm ele}$, $E_{\rm vib}^{400{\rm K}}$, $S_{\rm vib}^{400{\rm K}}$, and $G^{400{\rm K}} = E_{\rm ele} + E_{\rm vib}^{400{\rm K}} + pV - TS_{\rm vib}^{400{\rm K}}$ are the electronic energy at $T = 0$ K, the vibrational energy including the zero-point energy, the phonon entropy, and the Gibbs free-energy at $T = 400$ K, respectively. The electronic energy is measured in reference to the standard states of the atomic elements. 59

List of Figures

1.1 Schematic view of a Li-ion battery. 2

2.1 The relations of the projected distance x_{ik} and the integration of coordination number for each layered structure (AA or AB) when atom i is projected on the neighboring layer. Red, green, blue, and cyan lines correspond to AB-sequence, AA-sequence, the mid of AB- and AA- sequence structures, respectively. . . 26

3.1 Crystal structure of diamond. Black sphere denotes the atoms adopted the QM calculation. 32

3.2 The time evolution of Hamiltonian, potential, and kinetic energy. 33

3.3 Atomic cluster model for the QM calculation of the cluster region in the hybrid QM-CL simulation for graphite. Brown, green, peach spheres depict carbon(C), buffer atom (C), and buffer atom (H), respectively. 34

3.4 The charge density distribution in the basal plane perpendicular to the inter-layer direction (c axis) in the cluster region applied the QM calculation for graphite. Brown, green, peach spheres depict carbon(C), buffer atom (C), and buffer atom (H), respectively. 35

3.5 Crystal structure model of Li-GIC in the hybrid QM-CL simulation . Red (Li) and black (C) sphere depicts atoms included the QM cluster region. Gray spheres show the CL-C atoms. 36

3.6 The valence charge-density distribution around the Li atom in (0100) plane. The large red, gray and small black spheres indicate Li, C and quantum-calculated C atoms, respectively. 37

3.7 Before and after the change of the cluster region, the forces acting Li and C atoms around it. Red (Li) and black (C) sphere depicts atoms included the cluster region. 38

3.8 A snapshot of Li diffusion process provided from a hybrid calculation at temperature of $T = 398$ K. Red, black, and white spheres are Li, QM-calculated C, and CL-calculated C atoms, respectively. Trajectory of Li is also drawn. (a)Top view. (b)Side view. The letters of "A" or "B" denote the stacking structure of C-layers. 39

3.9 Time evolution of mean square displacements of Li at temperature $T = 398K$. Dot straight line shows the line approximated for the calculation of the diffusion coefficient. . 39

3.10 (a)The time evolution of parameter Z which distinguishes AB-type from AA of the C layers in Li-GIC. (b,c)Trajectories of x coordinate of Li. Blue (magenta) line depicts in the case of one (two) Li atom(s). 40

4.1 The side $(x-y)$ view of the total simulation system. The large red and medium green spheres are respectively the Li and C atoms in the QM region. The small blue spheres are the C atoms in the CL region. 47

4.2 The averaged inter-layer distance of the graphite at equilibrium as a function of temperature T (K), obtained through separate classical MD simulation. The solid line shows the fitting formula $f(T) = 3.36(1 + 6.7 \times 10^{-5}T)$. . . . 49

4.3 The valence-electron density on a y-plane in the QM region obtained in the hybrid QM-CL simulation. The black sphere is the Li ion, while the gray spheres the C atoms. The density less than 0.001 a.u.$^{-3}$ is omitted. 50

4.4 The mean square displacements of the Li ion as functions of time in the hybrid QM-CL simulation at 423 K for the compressed (-3.9% and -1.7%), equilibrium (0.6%), and stretched (2.9%) values of L_z. For better statistics, the time origins are set at every 0.1 ps in the simulation run of total 12 ps. 52

4.5 The trajectory of the Li ion during 10 ps viewed from z-direction, obtained in the hybrid QM-CL simulation. The four cases of the change of L_z are considered. The initial position of the Li ion is depicted by the open arrow. The final position by the large red sphere. The green spheres are the C atoms in the QM region. The black arrows depict the places where the Li ion passes through the places at which two C atoms belonging to different layers assume the same $x - y$ positions. 54

4.6 The Li ion at the ground and transition states in the hopping diffusion in the graphite. The Li ion is sandwiched by two C-layers. 55

4.7 The activation energy for the hopping diffusion of the Li ion in the graphite at $T = 0$ K calculated using the hybrid QM-CL simulation method. The filled circles with the black curve represent the data evaluated using the total energy. The open circles with the gray curve represent the data using the energy of the QM region only. The strain corresponds to the variation of L_z from the equilibrium distance of 26.97 Å at 0 K. The error bars indicate the estimated overall errors relating to the convergence fluctuation in the real-space DFT method. 57

4.8 The local strains as functions of L_z calculated using the hybrid QM-CL simulation method at $T = 0$ K. The open blue spheres are for the region near the Li ion; the filled red spheres, for the region far from the Li ion. The black line represents the ideal case of uniform strain. 58

4.9 Schematic illustration of the phase boundary of the random-stage and stage-4 structures in the Li-GIC. The blue horizontal lines indicate the graphite layers. The stresses acting on the layers due the differences in the inter-layer distance, are depicted by the arrows. 61

5.1 Top (x-y) and side (x-z) views of simulation system in hybrid QM-CL simulation run at $T = 423$ K with zero external electric field. The large and medium spheres are respectively the Li and C atoms in the QM region. The small spheres with bonds are C atoms in the CL region. The curve is the trajectory of the Li ion for the 10 ps obtained in the simulation run. The large arrow depicts the initial position of the Li ion. The small arrows indicate the places where the changes between the hopping and ballistic modes occur during the migration. The C-Li distances $d_{\rm u}$ and $d_{\rm l}$ are depicted. . . 66

5.2 Diffusion behavior of Li ion in graphite at $T = 423$ K with zero external electric field, observed in hybrid QM-CL simulation run. The time evolutions of the external electric field, $d_{\rm u}$ and $d_{\rm l}$, and the absolute values of the Li displacements in three directions are depicted in top, middle, and bottom panels, respectively. 70

5.3 Time evolutions of mean squared displacements of Li ion obtained in hybrid QM-CL simulation runs at $T = 423$ K with various external electric fields. For better statistics, the time origins are set every 10 fs in a total simulation period of 5 ps. 71

5.4 Same as Fig. 5.2, but with the external electric field amplitude $E_z^{\rm amp} = 0.43$ V/Å. (a) At frequency $f = 0.4$ THz. (b) At $f = 1.7$ THz. 73

Chapter 1

Introduction

1.1 Motivation

The global warming that has been guessed to be caused by the emission of greenhouse gas as carbon dioxide and the exhaustion of fossil fuel itself, are going to limit social growth and flourish. The challenges in moving towards renewable energy resources such as the solar power, wind power generation, and biomass fuel have been addressed in both academic and commercial societies. Under the situation, automakers have accelerated the development and practical applications of green vehicles or environmentally friendly vehicles, for example, hybrid cars (HV), plug-in hybrids (PHV), electric cars (EV), and fuel cell-powered hydrogen cars (FC). Rechargeable batteries are indispensable for these green vehicles, and the research and development have focused on the lithium (Li) ion rechargeable battery. The Li-ion rechargeable battery provides higher energy density compared to the various other known rechargeable battery systems such as lead-acid, nickel-cadmium, and nickel-metal hydride batteries. In the Li-ion battery, the Li ions are shuttled between the positive and negative electrodes by the applied voltage through the nonaqueous electrolyte and separator as shown in Fig. 1.1. Such charge and discharge reactions involve following key processes: the transport of the Li ions in both electrode and electrolyte materials, the charge transfer at the electrolyte-electrode interfaces, and the internal structural changes of the electrodes relating to the increase in the Li density. Various requirements exist to advance the power, capacity, recharging speed,

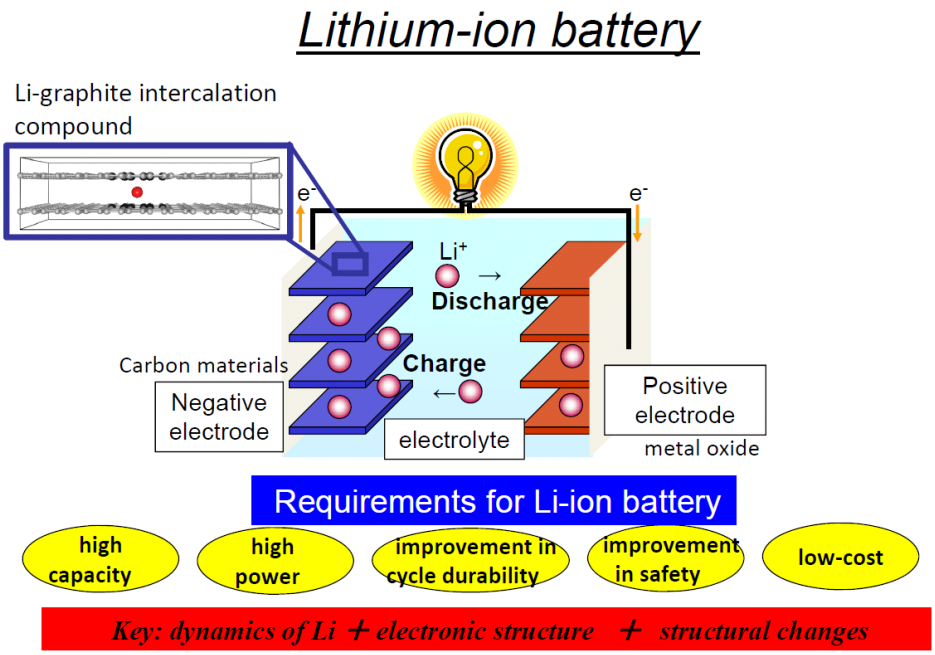

Figure 1.1: Schematic view of a Li-ion battery.

and durability of the Li-ion battery.

Intercalation compounds are used in the Li-ion batteries [1]. Metal-oxides like lithiated Co oxides ($LiCoO_2$) have become attractive positive electrodes. While, graphite forms intercalation compounds with some metals or small molecules inserted between its layers. The Li-graphite intercalation compound (Li-GIC) is put to practical use as a negative electrode of the Li-ion battery. Basically, the charge-discharge reactions of Li-ion batteries involve: the migration of Li ions in the electrode and electrolyte materials, the charge transfer at their insertion into (or extraction from) the host electrodes, and the structural changes of electrodes. The transport properties of Li in the graphite layers particularly affect the power performance of Li-ion batteries, and the knowledge of diffusion process is required for the design and optimization of Li-ion batteries. In order to understand the mechanism of Li diffusion in more detail, it is essential to clarify the overall relation between the bonding nature of Li with carbon (C) atoms in the graphite and its structural change. From the theoretical point of view, the coupled calculation should be performed in focusing on not only the static properties

such as the electronic structure on the Li-GICs but also the dynamics of Li simultaneously.

Large, multi-scale simulation has been attracting much attention as one of the systematic methods that meet the situation mentioned above, where we cannot separate the macroscopic dynamical behavior of the whole system and the microscopic processes at electronic level. Generally, the classical molecular dynamics (MD) simulations based on an empirical atomic interaction potential model for large systems can be handled on parallel machines with order-N algorithm. However, the classical MD cannot treat the chemical reaction such as the formation or scission of chemical bonds. On the other hand, the computational efficiency of the first-principles MD technique which treats not only electronic states by using the quantum-mechanical (QM) theory but also time evolution of atoms has greatly increased, but the system scale is still limited. Further improvement of the performance of computer is desirable to apply this technique to the system of real scale. Thus hybrid quantum (QM)-classical (CL) simulation schemes have attracted great attention as they are aiming at both large-scale and high accuracy. In the scheme, the reaction region where the electronic structure should be treated by a highly accurate calculation technique such as the density functional theory (DFT), and this region is embedded in a CL system of atoms described with an empirical interaction model. It is expected that we can simulate the realistic large-scale system to reproduce the physical phenomenon of our interest by using the hybrid scheme. It is a very active area of research and some relevant methods have been proposed, perhaps the most popular one is ONIOM [2]. However, insufficient accuracies are observed, especially when it is applied to three-dimensional materials.

In this study, we apply originally developed hybrid QM-CL simulation code to analyze the diffusion process of the Li ion in Li-GICs. The region including the inserted Li and neighboring C atoms is treated with electronic state by the DFT code implemented with the finite difference method. On the other hand, the classical MD method using empirical interatomic potential is adopted to the movement of the rest C atoms of graphite. Buffered cluster method (BCM) [3], which is a technique suited to couple the QM and CL regions in three-dimensional materials, is applied.

The rest of the present thesis is organized as follows. The following three sections in this chapter present a brief outline of the theory on MD, DFT, and BCM, which are the foundations of the present code. In Chap. 2, we will describe the details of the interatomic interaction model between C atoms used in the CL calculation. Chapter 3 will report the simulation results on the preparatory calculations when the hybrid QM-CL simulation technique is applied to the Li-GIC. A series of the hybrid QM-CL simulation runs on stress-dependence of Li diffusivity in graphite at temperature of 423 K will be performed in Chap. 4. We will discuss about the relation between the inter-layer distance and the Li diffusivity. Possible explanation for the significant lowering of the Li diffusivity observed experimentally at the situation of mixed stage-structures will be given. In Chap. 5, we will analyze the relation between the vertical position and diffusivity of the Li ion in graphite. Motivated by the results of the present analyses, we will perform additional hybrid simulation to demonstrate enhanced thermal diffusivity of the Li ion by applying various settings of the amplitude and frequency of alternating electric fields perpendicular to C-layers. The summary of the present study will be shown in Chap. 6.

1.2 Molecular dynamics for classical (CL) dynamics calculation

The molecular dynamics (MD) calculation is one of the most basic materials simulation tools. This technique is used for the study of many physical chemistry phenomena in fluid, phase transition, droplet, etc. In this section, only the basic introduction is described.

1.2.1 Molecular dynamics

The most important point of the MD scheme is how to describe the interatomic interaction, or how to incorporate electronic structural change as a hidden variation. The first-principles MD simulation method with interatomic interaction calculated on the fly from the electronic structure, is still time-consuming. Therefore, the classical MD method which uses

potentials based on experimental data or the independent electronic structure calculation is popular. The interaction is usually divided into two-body, three-body, and many-body terms, they may be long-ranged or short-ranged; each term is represented by a useful function form.

The MD simulation begins by initialization of the atomic positions and velocities. For a crystal solid, for example, the initial positions will be determined by an atomic position in the unit cell and its spatial copies in the crystal symmetry. Then the simulation cell contains the repeated unit cells. The initial velocities are set by assuming Maxwell-Boltzmann distribution along the three dimensions. This is provided by the Gaussian distributed random numbers multiplied by the mean velocity given by $\sqrt{2k_BT/m}$, where k_B is Boltzmann constant, T is temperature, and m is atomic mass, under the condition that total atomic momenta are zero. When this initialization is made for given temperature once, total energy of the system is conserved.

The MD algorithm to be mentioned in the next subsection has the time reversal symmetry. Therefore, unlike the Monte Carlo method, if a set of positions and velocities is given first, MD is a deterministic method in that the time evolution is completely determined from its current state.

Statistical mechanics is used in order to extract macroscopic information from the microscopic one provided by the MD simulations. It is based on the concept that many individual microscopic configurations in a large system lead to the same macroscopic properties after long time simulations. In other words, it is not necessary to save all the detailed trajectories of every particle (atom) in the system in order to predict the physical properties. Usually the statistical ensemble is characterized by fixing the thermodynamic variables (e.g., total energy E, temperature T, pressure P, volume V, number of atoms N, or chemical potential μ). There are various types of statistical ensembles depending on variables kept fixed. The microcanonical ensemble is characterized by constant N, V, and E, and denoted as NVE ensemble. Other important ensembles include the canonical (NVT) ensemble, the isothermal-isobaric or NPT ensemble, and the grand-canonical (μVT) ensemble. The thermodynamic variables which define an ensemble can be considered as control parameters when a simulation run is carried out.

1.2.2 Time integration of equation of motion

Various techniques to integrate the equation of motion have been developed. One of the simplest and robust algorithms is the Verlet method. Assume that time evolution of position $\boldsymbol{x}$ is represented by the Taylor expansion as follows:

$$\boldsymbol{x}(t+\delta t) = \boldsymbol{x}(t) + \boldsymbol{v}(t)\delta t + \frac{\boldsymbol{F}(t)}{2m}\delta t^2 + \cdots, \tag{1.1}$$

where $\boldsymbol{v}$ is velocity and $\boldsymbol{F}$ denotes force. Similarly, the velocity $\boldsymbol{v}$ is expressed as

$$\boldsymbol{v}(t+\delta t) = \boldsymbol{v}(t) + \frac{\boldsymbol{F}(t)}{m}\delta t + \cdots, \tag{1.2}$$

$$\boldsymbol{v}(t) = \boldsymbol{v}(t+\delta t) - \frac{\boldsymbol{F}(t+\delta t)}{m}\delta t + \cdots. \tag{1.3}$$

These equations lead to following formula:

$$\boldsymbol{v}(t+\delta t) = \boldsymbol{v}(t) + \frac{\boldsymbol{F}(t+\delta t) + \boldsymbol{F}(t)}{2m}\delta t. \tag{1.4}$$

When initial position $\boldsymbol{x}(0)$ and velocity $\boldsymbol{v}(0)$ are given, their time evolutions are obtained by updating a time step to $\boldsymbol{x}(t+\delta t)$, $\boldsymbol{F}(t+\delta t)$, and $\boldsymbol{v}(t+\delta t)$.

The instantaneous temperature $T(t)$ with atomic mass m_i and velocity $\boldsymbol{v}_i$ of atom i is defined in the following:

$$\frac{3}{2}Nk_BT(t) = \sum_{i=1}^{N}\frac{m_i\boldsymbol{v}_i^2}{2}, \tag{1.5}$$

where N represents the number of atoms in simulation system. Therefore, setting temperature to T_0 is realized by the velocity scaling, that is each atomic velocity is multiplied by the same factor

$$\lambda = \sqrt{\frac{T_0}{T(t)}}. \tag{1.6}$$

1.3 Density functional theory for quantum (QM) calculation

1.3.1 Basis of theory

The density functional theory (DFT) is a method used most widely for electronic structure calculations of materials today, and it is formulated

following the idea by Kohn-Sham in 1965 [4]. They propose to replace the originally many-body interacting system with the supported independent (no-interacting) electron system. Various trial calculations demonstrated high accuracies the properties of interesting systems predicted by the DFT method. In this section, we explain the basic formulation of the Kohn-Sham method and a way of thinking about the exchange-correlation energy functional which is the most important element.

The Hamiltonian of the system consisting of electrons and nuclei that interact through the Coulomb potential is

$$\begin{aligned}\hat{H} = -\frac{1}{2}\sum_i \nabla_i^2 \quad &- \quad \sum_{i,I} \frac{Z_I}{|\boldsymbol{r}_i - \boldsymbol{R}_I|} + \frac{1}{2}\sum_{i\neq j} \frac{1}{|\boldsymbol{r}_i - \boldsymbol{r}_j|} \\ &- \quad \sum_I \frac{1}{2M_I}\nabla_I^2 + \frac{1}{2}\sum_{I\neq J} \frac{Z_I Z_J}{|\boldsymbol{R}_I - \boldsymbol{R}_J|}. \end{aligned} \tag{1.7}$$

The atomic unit ($\hbar = m_e = e = 1$) is adopted, and the electron is expressed by a subscript using a small letter; atomic nucleus having mass M_I and electronic charge Z_I is denoted in the subscript using a capital letter. The ratio $\frac{m_e}{M_I}$ of electronic mass m_e and the nuclear mass is quite small. We can separate the motion of nucleus and electronic wave function as the ratio is small. This is the essence of the Born-Oppenheimer approximation or an adiabatic approximation.

The following is provided as Hamiltonian of the electronic system under Born-Oppenheimer approximation:

$$\hat{H} = \hat{T} + \hat{V}_{ext} + \hat{V}_{int} + E_{II}. \tag{1.8}$$

The kinetic operator for electrons is

$$\hat{T} = -\frac{1}{2}\sum_i \nabla_i^2. \tag{1.9}$$

The attractive interaction from the nuclei is

$$\hat{V}_{ext} = \sum_{i,I} V_I(|\boldsymbol{r}_i - \boldsymbol{R}_I|) = -\sum_{i,I} \frac{Z_I}{|\boldsymbol{r}_i - \boldsymbol{R}_I|}, \tag{1.10}$$

the electron-electron interaction is

$$\hat{V}_{int} = \frac{1}{2}\sum_{i\neq j} \frac{1}{|\boldsymbol{r}_i - \boldsymbol{r}_j|}, \tag{1.11}$$

and the classical Coulomb interaction between nuclei is

$$E_{II} = \frac{1}{2}\sum_{I\neq J}\frac{Z_I Z_J}{|\boldsymbol{R}_I - \boldsymbol{R}_J|}, \tag{1.12}$$

which contributes to the total energy of system, but has nothing to do with the electronic state directly.

The DFT is based on the Hohenberg-Kohn theorems:

- For a system interacting in the external potential V_{ext}, the ground state properties of the system are uniquely determined by the ground-state electron density.
- An energy functional for the system is defined as functional of electron density ρ and the correct ground state electron density minimizes this energy functional:

$$E[\rho] = F[\rho] + \int \mathrm{d}\boldsymbol{r} V_{ext}(\boldsymbol{r})\rho(\boldsymbol{r}) + E_{II}, \tag{1.13}$$

$$F[\rho] = T[\rho] + E_{int}[\rho]. \tag{1.14}$$

The Kohn-Sham method reduces mathematically the interacting electron system, which is hard to be treated, with a non-interacting electron system in some effective potential under the condition that the electron density is the same.

The Hamiltonian of the independent electron system is represented as:

$$H = -\frac{\nabla^2}{2} + V(\boldsymbol{r}). \tag{1.15}$$

The solution for an electronic state is obtained from

$$\left[-\frac{\nabla^2}{2} + V(\boldsymbol{r})\right]\psi_i(\boldsymbol{r}) = \varepsilon_i\psi_i(\boldsymbol{r}). \tag{1.16}$$

The electron is fermion having spin 1/2. Hence the total electronic state, which obeys the Pauli principle, is given by the Slater determinant of $\{\psi_i\}$. The electron density of independent system of N electrons is expressed by the sum of squares of orbitals:

$$\rho(\boldsymbol{r}) = \sum_{i=1}^{N}|\psi_i(\boldsymbol{r})|^2. \tag{1.17}$$

The kinetic energy T_s of the independent electrons under the condition that $\rho(\boldsymbol{r})$ is the same with that of the original system is given by

$$T_s = -\frac{1}{2}\sum_i \langle\psi_i|\nabla^2|\psi_i\rangle. \tag{1.18}$$

Furthermore, the classical Coulomb interaction energy of interacting electron density $\rho(\boldsymbol{r})$ is defined in the following:

$$E_{hartree} = \frac{1}{2}\int \frac{\rho(\boldsymbol{r})\rho(\boldsymbol{r}')}{|\boldsymbol{r}-\boldsymbol{r}'|}\mathrm{d}\boldsymbol{r}\mathrm{d}\boldsymbol{r}'. \tag{1.19}$$

In the Kohn-Sham method the energy functional in the ground state corresponding to Eq.(1.13) is written exactly as follows:

$$E_{KS} = T_s[\rho] + \int \mathrm{d}\boldsymbol{r} V_{ext}(\boldsymbol{r})\rho(\boldsymbol{r}) + E_{hartree}[\rho] + E_{II} + E_{xc}[\rho]. \tag{1.20}$$

The kinetic energy of non-interacting electrons T_s is provided by functional formula of orbitals explicitly. All the remaining many-body interaction effects are included in the exchange-correlation energy term E_{xc}.

The Exchange-correlation energy functional E_{xc} can be written as follows by comparing Eq.(1.13) and Eq.(1.20):

$$E_{xc}[\rho] = T[\rho] - T_s[\rho] + E_{int}[\rho] - E_{hartree}[\rho]. \tag{1.21}$$

Because the right-hand side of this equation is functional of electron density ρ, E_{xc} is also functional. If functional energy E_{xc} is given, ground state energy and electron density of many-body problem will be obtained by solving Kohn-Sham equation for non-interacting electron system. Equation(1.21) shows that the differences between T and T_s and a non-classical part of the electron-electron interaction energy are included in the exchange-correlation energy. Thus, if the energy E_{xc} is known as a functional of the density, these form a closed set of self-consistent equations yielding the exact answer to the electronic structure problem, without treating complicated electron-electron repulsion directly.

1.3.2 Kohn-Sham equation

In order to get the set of wave functions $\{\psi_i\}$ in the ground state, which are orthogonal because of the usage of the Slater determinant, Eq.(1.20) is

minimized with respect to ψ_i^* under the normalization condition

$$\langle \psi_i | \psi_i \rangle = 1 \tag{1.22}$$

as

$$\frac{\delta}{\delta \psi_i^*(\boldsymbol{r})} \left[E_{KS} - \sum_j \varepsilon_j \left\{ \langle \psi_j | \psi_j \rangle - 1 \right\} \right] \tag{1.23}$$

$$= \frac{\delta T_s}{\delta \psi_i^*(\boldsymbol{r})} + \left[V_{ext}(\boldsymbol{r}) + \frac{\delta E_{hartree}}{\delta \rho(\boldsymbol{r})} + \frac{\delta E_{xc}}{\delta \rho(\boldsymbol{r})} \right] \frac{\delta \rho(\boldsymbol{r})}{\delta \psi_i^*(\boldsymbol{r})} - \varepsilon_i \psi_i(\boldsymbol{r}) \tag{1.24}$$

$$= 0. \tag{1.25}$$

Since

$$\frac{\delta T_s}{\delta \psi_i^*(\boldsymbol{r})} = -\frac{1}{2} \nabla^2 \psi_i(\boldsymbol{r}) \tag{1.26}$$

and

$$\frac{\delta \rho(\boldsymbol{r})}{\delta \psi_i^*(\boldsymbol{r})} = \psi_i(\boldsymbol{r}), \tag{1.27}$$

the following Kohn-Sham (KS) equation is obtained:

$$H_{KS} \psi_i(\boldsymbol{r}) = \varepsilon_i \psi(\boldsymbol{r}), \tag{1.28}$$

$$H_{KS} = -\frac{1}{2} \nabla^2 + V_{KS}(\boldsymbol{r}) \tag{1.29}$$

with

$$V_{KS}(\boldsymbol{r}) = V_{ext}(\boldsymbol{r}) + \frac{\delta E_{hartree}}{\delta \rho(\boldsymbol{r})} + \frac{\delta E_{xc}}{\delta \rho(\boldsymbol{r})} \tag{1.30}$$

$$= V_{ext}(\boldsymbol{r}) + V_{hartree}(\boldsymbol{r}) + V_{xc}(\boldsymbol{r}). \tag{1.31}$$

The Kohn-Sham equation has the form of the independent electron equation. The potential and the electron density are solved numerically through the self-consistent field (SCF) iteration [5, 6, 7] under the orthonormalization constraint. These equations are independent of the approximation for functional $E_{xc}[\rho]$ formula, and give the strict energy and electron density of the ground state for the interacting system only if the exact $E_{xc}[\rho]$ form is known.

An electron will move in the Coulomb field provided by nuclei. The effect on electron from nuclei is included in the fixed potential for the electron. It is established even if naked nuclear Coulomb interaction is replaced with the psudopotential in which the core electrons are removed and only valence

electron interaction can be described. Other external potential such as electric fields can be taken in easily. Let us consider an atomic cluster composed of $N_{\rm ion}$ ions with charge numbers $\{Z_I\}$ for the I-th atoms and the valance electrons. For simplicity, the charge-neutral system is assumed though the formulation is applicable to non-neutral systems also; the total number of electrons $N_e = \sum_I Z_I$.

The pseudopotential of ion-I, $v_{{\rm ion},I}(\boldsymbol{r})$, for wave function $\psi_i(\boldsymbol{r})$ acts as

$$v_{{\rm ion},I}(\boldsymbol{r})\psi_i(\boldsymbol{r}) = v_{{\rm L},I}(\boldsymbol{r})\psi_i(\boldsymbol{r}) + v_{{\rm NL},I}(\boldsymbol{r})|\psi_i\rangle \tag{1.32}$$

with

$$v_{{\rm NL},I}(\boldsymbol{r})|\psi_i\rangle = \sum_{l=0}^{l_{\max}} \sum_{m=-l}^{l} \frac{\psi^{\rm ps}_{lm,I}(\boldsymbol{r})\Delta v_{l,I}(\boldsymbol{r}) \int d\boldsymbol{r}' \psi^{\rm ps*}_{lm,I}(\boldsymbol{r}')\Delta v_{l,I}(\boldsymbol{r}')\psi_i(\boldsymbol{r}')}{\int d\boldsymbol{r} \psi^{\rm ps*}_{lm,I}(\boldsymbol{r})\Delta v_{l,I}(\boldsymbol{r})\psi^{\rm ps}_{lm,I}(\boldsymbol{r})} \ . \tag{1.33}$$

Here the Kleinman-Bylander form [8] is adopted for the treatment of the non-local pseudopotential. The $\psi^{\rm ps}_{lm,I}(\boldsymbol{r})$ in Eq. (1.33) is the pseudo eigen-orbital for a free atom-I at angular state denoted (l, m). The pseudopotential at a chosen angular state $l = l_{\rm loc}$ (often the maximum of l) is regarded as the local pseudopotential, and the deviation of the pseudopotential from the local one as the non-local pseudopotential:

$$v_{{\rm L},I}(\boldsymbol{r}) \equiv v_{l_{\rm loc},I}(\boldsymbol{r}) \ \text{ and } \ \Delta v_{l,I}(\boldsymbol{r}) \equiv v_{l,I}(\boldsymbol{r}) - v_{l_{\rm loc},I}(\boldsymbol{r}) \tag{1.34}$$

with the pseudopotential $v_{l,I}(\boldsymbol{r})$ for a free ion-I at angular state l. The $v_{{\rm L},I}(\boldsymbol{r})$ contains the long-ranged Coulomb potential, while the $\Delta v_{l,I}(\boldsymbol{r})$ is short-ranged one.

The Hartree potential in Eq. (1.31) is

$$V_{\rm hatree}(\boldsymbol{r}) = \int d\boldsymbol{r}' \frac{\rho(\boldsymbol{r}')}{|\boldsymbol{r} - \boldsymbol{r}'|} \tag{1.35}$$

or determined by solving the Poisson equation:

$$\nabla^2 V_{\rm hatree}(\boldsymbol{r}) = -4\pi\rho(\boldsymbol{r}) \tag{1.36}$$

with the density of electrons

$$\rho(\boldsymbol{r}) = \sum_{i=1}^{N_e/2} 2|\psi_i(\boldsymbol{r})|^2 \tag{1.37}$$

in the spin neutral case.

The $V_{xc}(\boldsymbol{r})$ in Eq. (1.31) is the exchange-correlation potential defined as the functional derivative of the exchange-correlation energy:

$$V_{xc}(\boldsymbol{r}) = \frac{\delta E_{xc}(\rho)}{\delta \rho(\boldsymbol{r})} \ . \tag{1.38}$$

Various approximation formulas of $E_{xc}(\rho)$ are given in literatures. The simplest approximation of the exchange correlation energy term is a local density approximation (LDA) in Ref. [9]:

$$E_{xc}^{LDA} = \int d\boldsymbol{r} \varepsilon_{xc}[\rho]\rho(\boldsymbol{r}), \tag{1.39}$$

$$V_{xc}^{LDA} = \varepsilon_{xc}[\rho] + \frac{\delta \varepsilon_{xc}}{\delta \rho}\rho. \tag{1.40}$$

Here, $\varepsilon_{xc}[\rho]$ is the exchange-correlation energy per unit volume of a homogeneous electron liquid of density $\rho(\boldsymbol{r})$.

The number of SCF iterations required to reach the convergence, which is independent of the target system size, is typically twenty. In the planewave-based KS-DFT method, eigen orbitals are represented using the planewaves under the periodic boundary conditions. And the SCF iteration procedure contains the local iteration for all the energy levels considered. In sweeping the orbitals for a given $\rho(\boldsymbol{r})$ in the local iteration procedure, orbitals are updated one by one from the lowest to highest energy levels by the conjugate gradient method with the Gram-Schmidt orthonormalization [10] to the orbitals at lower energy levels. Relating to the orthonormalization constraint, the number of numerical operations in the planewave-based KS-DFT method scales as order-N^3.

1.3.3 Real space implementation

In this subsection we present a real-space approach to the density functional calculations. In the real space density functional theory (RSDFT) method, we set the Cartesian mesh points in three-dimensional with the mesh size h to describe the eigen orbitals and the potentials. Therefore RSDFT has advantages to be able to set arbitrary boundary conditions compared with other conventional methods such as the planewave-based one. The mesh size h in unit of the Bohr radius $a_{\mathrm{B}} \approx 0.529$ Å corresponds to the cutoff

energy $0.5(\pi/h)^2$ (a.u.) (1 a.u. of energy $\approx$ 27.2 eV) in the planewave-based KS-DFT method. The overall shape of the mesh points is spherical with radius $r_{\max}$, which is determined to enclose all the ions with a few Å vacuum width so that $\rho(\boldsymbol{r}) = 0$ at $r = r_{\max}$. The second derivative operations in the three directions in the KS and Poisson equations are calculated by the high-order (fourth or more) finite difference method [10, 11, 12, 13] using the data on multiple mesh points in both plus and minus sides. For the ion with relatively deep pseudopotential as oxygen, a smaller mesh size of $h/3$ is used at around the ion only to represent the pseudopotential accurately [14].

For the grid space h, the physical coordinate of each point is expressed in the following:

$$\begin{aligned} \boldsymbol{r}(i,j,k) &= (ih, jh, kh), & (1.41)\\ i &= \{1, \cdots, N_x\}, \quad j = \{1, \cdots, N_y\}, \quad k = \{1, \cdots, N_z\}. & (1.42) \end{aligned}$$

A trapezoid rule for numerical integral is used as

$$\int d\boldsymbol{r} f(\boldsymbol{r}) \doteq h^3 \sum_{ijk} f(\boldsymbol{r}(i,j,k)). \tag{1.43}$$

The value of the wave function and the electron density distribution are given only on discretized points in the real space finite difference method. Therefore, the Kohn-Sham equation is given in a discretized form in the real space. Here, a procedure of discretization of the Kohn-Sham Hamiltonian is described in conformity with a finite difference approximation.

A key aspect is the availability of higher order expansions for the kinetic energy operator, i.e., expansions of the Laplacian. If we impose a simple and uniform grid on our system where the grid points are described by (x_i, y_j, z_k), we may write

$$\frac{\partial^2 \psi}{\partial x^2} = \sum_{n=-N}^{N} C_n \psi(x_i + nh, y_j, z_k) + O(h^{2N+2}), \tag{1.44}$$

where h is the grid spacing. The approximation is accurate to $O(h^{2N+2})$ upon the assumption that ψ can be approximated accurately by a power series in h. Algorithms are available to compute the coefficients C_n for arbitrary order in h. For example, in the case of $N = 2$ the coefficients C_n are provided as

follows:

$$C_{-2} = C_2 = -\frac{1}{12h^2}, \tag{1.45}$$

$$C_{-1} = C_1 = \frac{4}{3h^2}, \tag{1.46}$$

$$C_0 = -\frac{5}{2h^2}. \tag{1.47}$$

The three-dimensional Kohn-Sham equation can be summarized following the argument mentioned above as

$$\begin{aligned} - \frac{1}{2}\Bigg[& \sum_{n_1=-N}^{N} C_{n_1}\psi(x_i + n_1 h, y_j, z_k) \\ & + \sum_{n_2=-N}^{N} C_{n_2}\psi(x_i, y_j + n_2 h, z_k) \\ & + \sum_{n_3=-N}^{N} C_{n_3}\psi(x_i, y_j, z_k + n_3 h)\Bigg] \\ & + V_{eff}(x_i, y_j, z_k)\psi(x_i, y_j, z_k) = \varepsilon\psi(x_i, y_j, z_k), \end{aligned} \tag{1.48}$$

$$\begin{aligned} & V_{eff}(x_i, y_j, z_k) \\ = \; & V_{ext}(x_i, y_j, z_k) + V_{hartree}(x_i, y_j, z_k) + V_{xc}(x_i, y_j, z_k), \end{aligned} \tag{1.49}$$

for each grid point (x_i, y_j, z_k). If there are M grid points, the size of the full matrix resulting from the above eigenvalue problem is $M \times M$. Here V_{ext} is the ionic pseudopotential, $V_{hartree}$ is the Hartree potential, and V_{xc} is the local density expression for the exchange and correlation potential. The two fixed grid parameters used in setting up the matrix are the grid spacing h and the order N.

The RSDFT method is well suited to the parallel computation environment. It is free from the fast Fourier transform (FFT) method, which occupies most of the calculation cost in conventional plane wave expansion method. The idea of spatial decomposition of the mesh points also works well for parallel machines. In addition, the RSDFT method has a unique feature of numerical stability that helps to realize high computational performance of the Gram-Schmidt orthonormalization of the orbitals as explained below. While the Gram-Schmidt orthonormalization needs to be performed orbital-by-orbital for stability reasons in the planewave-based

method, it can be performed for all the orbitals together in the RSDFT method after the orbital sweep in the local iteration procedure [13]. The rearrangement of the Gram-Schmidt orthonormalization procedure improves the computational performance [13] on a parallel machine by employing a highly tuned linear-algebra library.

1.4 Hybrid quantum classical simulation

The hybrid quantum (QM)-classical (CL) simulation is expected as one of the calculation methods aiming at both large-scale and high accuracy. In this method, the reaction region, where the electronic structure is treated by a highly accurate calculation technique such as the DFT, is embedded in a classical dynamics system of atoms based on an empirical interaction model. In the hybrid QM-CL simulation, the atomic bond is cut at the QM-CL boundary and dangling bond forms. As for this dangling bond, its influence on electronic state or bonding distance of the atoms in the QM region should be removed. The link-atom (or handshake atom) method [15] that uses hydrogen atoms for termination of the QM atoms is usually applied to couple the QM and CL regions. By using link-atom method, however, there is the case that influence of the surface reconstruction with the relaxation of the boundary atom extends to the atoms of whole system and a large distortion from the original stable structure is produced. In this study, we adopt the buffered cluster method (BCM) [3], which requires no link-atoms and is more precise and a general-purpose model. In following subsection we present outline of the BCM.

1.4.1 Buffered cluster method

In the BCM, additional atoms called buffer atoms are put to terminate the dangling bond of the QM atoms at QM-CL boundaries. The positions of the buffer atoms are adjusted so as to minimize the potential energy under the constraint of fixing the position of the QM atoms for the CL calculation of the QM cluster region. In the QM calculation, the positions of the buffer atoms are not relaxed. Therefore various surface reconstructions of the QM cluster

region are suppressed in the BCM. The demonstrations for simulation about the stress corrosion clacking mechanism of silicon and the alumina make this technique be practical [3].

Among target system, we assume a region dealt with by the QM calculation as cluster region. The subscript CL denotes the physical properties calculated from the CL calculation, or QM denotes ones computed from the QM calculation.

In the hybrid QM-CL simulation, the Hamiltonian of the system is defined as follows:

$$H(\boldsymbol{R}_{\rm all}, \boldsymbol{P}_{\rm all}) = H_{\rm CL}^{\rm system}(\boldsymbol{R}_{\rm all}, \boldsymbol{P}_{\rm all}) + \sum_{\rm cluster} (E_{\rm QM}^{\rm cluster} - E_{\rm CL}^{\rm cluster}). \tag{1.50}$$

Here, $\boldsymbol{R}_{\rm all}$ and $\boldsymbol{P}_{\rm all}$ represent the position and momentum of all atoms, respectively. Hamiltonian $H_{\rm CL}^{\rm system}$ is obtained by applying the CL calculation to the whole system: $H_{\rm CL}^{\rm system} = E_{\rm kin}(\boldsymbol{P}_{\rm all}) + E_{\rm CL}^{\rm system}(\boldsymbol{R}_{\rm all})$. The last two terms in Eq. (1.50) are energies given from the QM and CL calculations in the cluster region, respectively.

We assume the group of an atomic position in the cluster region to be $\{\boldsymbol{r}_{\rm cluster}\}$. The energy term in the cluster region is given by the function depending on only $\boldsymbol{r}_{\rm cluster}$ in the BCM:

$$E_{\rm QM}^{\rm cluster} = E_{\rm QM}^{\rm cluster}(\{\boldsymbol{r}_{\rm cluster}\}), \tag{1.51}$$

$$E_{\rm CL}^{\rm cluster} = E_{\rm CL}^{\rm cluster}(\{\boldsymbol{r}_{\rm cluster}\}). \tag{1.52}$$

In the QM and CL calculations in the cluster region, additional atoms are set on the dangling bonds in order to terminate the bonds of the atoms in cluster which are cut on the boundary or surface of region. This additional atom is called 'buffer atom'.

The constituent atomic element of the system is used as the buffer atoms to mimic the original bonding in the CL calculation in the cluster region. The position of this buffer atom is adjusted under the condition of the atomic position $\boldsymbol{r}_{\rm cluster}$ in the cluster region fixing to minimize potential energy $E_{\rm CL}^{\rm cluster}$. In the QM calculation in the cluster region, the constituent atom or hydrogen atom is chosen as the buffer atom corresponding to the coordination number of original atom. Its position is provided with reference to a position of buffer atom determined by the CL calculation in the cluster region and not relaxed

when the QM calculation is conducted. If buffer atoms are relaxed in the QM calculation, there is the possibility of various surface reconstructions. When hydrogen atom is chosen as the buffer atom, its position $\{\boldsymbol{r}_{\mathrm{b}}\}$ is set to be $\boldsymbol{r}_{\mathrm{b}} = \beta \boldsymbol{r}_{\mathrm{CL}}^{\mathrm{buffer}} + (1-\beta)\boldsymbol{r}_{\mathrm{cluster}}$ with scaling factor β. On the other hand, in the case that the constituent atom is put as buffer atom, it becomes $\boldsymbol{r}_{\mathrm{b}} = \boldsymbol{r}_{\mathrm{CL}}^{\mathrm{buffer}}$.

The force to act on the atom in the cluster region is as follows:

$$\boldsymbol{F}_i = -\frac{\partial H}{\partial \boldsymbol{r}_{\mathrm{cluster},i}} \tag{1.53}$$

$$= -\frac{\partial E_{\mathrm{CL}}^{\mathrm{system}}}{\partial \boldsymbol{r}_{\mathrm{cluster},i}} - \sum_{\mathrm{cluster}} \left(\frac{\partial E_{\mathrm{QM}}^{\mathrm{cluster}}}{\partial \boldsymbol{r}_{\mathrm{cluster},i}} - \frac{\partial E_{\mathrm{CL}}^{\mathrm{cluster}}}{\partial \boldsymbol{r}_{\mathrm{cluster},i}} \right), \tag{1.54}$$

$$\frac{\partial E_{\mathrm{QM}}^{\mathrm{cluster}}}{\partial \boldsymbol{r}_{\mathrm{cluster},i}} = \left(\frac{\partial E_{\mathrm{QM}}^{\mathrm{cluster}}}{\partial \boldsymbol{r}_{\mathrm{cluster},i}} \right)_{\mathrm{fix}\ \{\boldsymbol{r}_{\mathrm{b}}\}} + \sum_{j}^{\mathrm{buffer}} \frac{\partial E_{\mathrm{QM}}^{\mathrm{cluster}}}{\partial \boldsymbol{r}_{\mathrm{b},j}} \left(\frac{\partial \boldsymbol{r}_{\mathrm{b},j}}{\partial \boldsymbol{r}_{\mathrm{cluster},i}} \right)_{\mathrm{CL}}, \tag{1.55}$$

$$\frac{\partial E_{\mathrm{CL}}^{\mathrm{cluster}}}{\partial \boldsymbol{r}_{\mathrm{cluster},i}} = \left(\frac{\partial E_{\mathrm{CL}}^{\mathrm{cluster}}}{\partial \boldsymbol{r}_{\mathrm{cluster},i}} \right)_{\mathrm{fix}\ \{\boldsymbol{r}_{\mathrm{b}}\}}. \tag{1.56}$$

Here $\{\boldsymbol{r}_b\}$ is the position of buffer atom, $\left(\frac{\partial \boldsymbol{r}_{\mathrm{b},j}}{\partial \boldsymbol{r}_{\mathrm{cluster},i}} \right)_{\mathrm{CL}}$ is provided from the numerical finite difference in the CL calculation in cluster region. Moreover, Eq. (1.55) includes the force term of buffer atom $\frac{\partial E_{\mathrm{QM}}^{\mathrm{cluster}}}{\partial \boldsymbol{r}_{\mathrm{b},j}}$ which is calculated from the QM calculation in the cluster region.

Atomic forces outside of the cluster region are given as the next formula, assuming their positions to be $\{\boldsymbol{r}_{\mathrm{env}}\}$:

$$\boldsymbol{F}_i = -\frac{\partial E_{\mathrm{CL}}^{\mathrm{system}}}{\partial \boldsymbol{r}_{\mathrm{env},i}}. \tag{1.57}$$

Chapter 2

Application for carbons

In this chapter we will describe the details of the potential models for carbons used in the classical MD simulation and their validity will be inspected.

2.1 Settings in CL calculation

In the hybrid QM-CL simulation method, the CL calculation is performed for the CL region, that is, the whole system minus the QM-cluster region. The velocity Verlet algorithm is used to integrate the Newton's equation of motion for all the atoms. The Brenner-type of interatomic potential [16] is adopted for the C atoms of the graphite. The Brenner type potential is useful for circumstances that have as single, double, conjugated double, and triple bond in the C-C bonding between carbon atoms, and has the Tersoff type potential [17] form.

We show below the formula of Brenner-type potential E and its derivative to be necessary for a calculation of the force. In addition, i and j are labels of the atoms, $r_{ij} = |\boldsymbol{r}_i - \boldsymbol{r}_j|$ is atomic distance, θ_{ijk} expresses bond angle between two vectors of $(\boldsymbol{r}_j - \boldsymbol{r}_i, \boldsymbol{r}_k - \boldsymbol{r}_i)$.

2.1.1 Brenner-type potential for intra-layer of carbons

Potential energy E is given as a sum of the binding energies between two atoms consisted of the repulsive term $V_R(r_{ij})$ and the attractive term $V_A(r_{ij})$:

$$E = \sum_i \sum_{j(j>i)} \left[V_R(r_{ij}) - \bar{B}_{ij} V_A(r_{ij}) \right]. \tag{2.1}$$

The many-body effect is taken in through the factor $\overline{B}_{ij}$ in front of the attractive potential term. The repulsive potential term $V_R(r)$ and attractive term $V_A(r)$ are considered to be exponential function formulas in reference to the Morse potential. They include the cutoff function $f_{ij}(r)$ which determines the interacting distance:

$$V_R(r) = f_{ij}(r)\frac{D}{S-1}\exp\left[-\sqrt{2S}\beta(r-R)\right], \tag{2.2}$$

$$V_A(r) = f_{ij}(r)\frac{DS}{S-1}\exp\left[-\sqrt{\frac{2}{S}}\beta(r-R)\right], \tag{2.3}$$

$$f_{ij}(r) = \begin{cases} 1, & r \le R^{(1)} \\ \frac{1}{2}+\frac{1}{2}\cos\left[\pi\frac{(r-R^{(1)})}{R^{(2)}-R^{(1)}}\right], & R^{(1)} < r < R^{(2)} \\ 0, & r \ge R^{(2)} \end{cases}. \tag{2.4}$$

Here, $R, D,$ and S are respectively the equilibrium distance of two-body interaction, the minimum value of the potential, and the ratio of working distance for attractive force to that for repulsive one. In the case of $S = 2$, these equations result in the Morse potential. The parameter β with a dimension of a reciprocal of distance is determined from the atomic force constant. The cutoff function $f_{ij}(r)$ is defined with the function form which the atomic interaction between atom i and j becomes zero smoothly. The distance $R^{(1)}$ decides the working range of the interatomic covalent bond, and there is no-interaction in $r \ge R^{(2)}$. Many-body interaction-effect factor $\overline{B}_{ij}$ makes B_{ij} symmetric. The correction term F_{CC} expressing π conjugate-bonding effect is added in symmetrization of B_{ij}:

$$\overline{B}_{ij} = \frac{1}{2}\left[(B_{ij}+B_{ji}) + F_{CC}(N_i, N_j, N_{ij}^{conj})\right], \tag{2.5}$$

$$B_{ij} = \left[1 + \sum_{k\neq i,j} G(\theta_{ijk}) f_{ik}(r_{ik}) \times \exp\left\{\alpha[(r_{ij}-R)-(r_{ik}-R)]\right\}\right]^{-\delta}, \tag{2.6}$$

$$G(\theta) = \alpha_0\left[1 + \frac{c_0^2}{d_0^2} - \frac{c_0^2}{d_0^2+(1+\cos\theta)^2}\right]. \tag{2.7}$$

The function form of B_{ij} is determined by the relations with the bond order and the coordination number of a local atom, and it depends on the bond angle and the bonding distance. Function $G(\theta)$ expresses the bond angle

dependence of B_{ij} and changes for a bond angle smoothly. Parameter c_0 decides strength of the influence from a bond angle, and d_0 determines the amount of change of the bond angle. Parameter α in the exponential function term in Eq.(2.6) reveals the range where the difference in two bonding distance r_{ij} and r_{ik} is taken into account. In correction term $F_{CC}(N_i, N_j, N_{ij}^{conj})$, N_i indicates the number of atoms combined with atom i.

Parameters used in this study are shown in Table 2.1, which are optimized to reproduce the binding energy and the equilibrium lattice constant of carbon based materials. In addition, the value of the correction term F_{CC} listed in paper of Brenner [16] is also written for reference. But the correction term F_{CC} is omitted in this study, because it is often left out in the calculation for the graphite and diamond.

We employ in Table 2.1 the same parameter values listed in Table I in Ref. [16] except for the equilibrium distance. The equilibrium distance is set to be 1.33116 Å so that the calculated equilibrium lattice constant of the graphite becomes equal to the one computed from the QM calculation, which is slightly longer than that in Ref. [16]. Such a fine tuning of the parameters in the CL potential is necessary in order not to create artificial stress at the QM-CL boundary in the hybrid QM-CL simulation method [18].

Table 2.1: Parameters of Brenner-type potential.

R [Å]	D [eV]	β [1/Å]	S	δ	α
1.33116	6.325	1.5	1.29	0.80464	0.0

$R^{(1)}$ [Å]	$R^{(2)}$ [Å]	α_0	c_0^2	d_0^2
1.7	2.0	0.011304	19^2	2.5^2

$F_{CC}(2,3,1)$	$F_{CC}(2,3,2)$	$F_{CC}(1,2,2)$	except for left
-0.0465	-0.0465	-0.0355	0

2.1.2 Derivatives of Brenner-type potential

The derivatives of Brenner-type potential which are needed in the calculation of atomic forces are complicated. For interested readers we here write down them explicitly as follows:

$$\frac{\partial E}{\partial \boldsymbol{r}_i} = \sum_{j(j>i)} \left[\frac{dV_R(r_{ij})}{dr_{ij}} \frac{\partial r_{ij}}{\partial \boldsymbol{r}_i} - \overline{B}_{ij} \frac{dV_A(r_{ij})}{dr_{ij}} \frac{\partial r_{ij}}{\partial \boldsymbol{r}_i} - V_A(r_{ij}) \frac{\partial \overline{B}_{ij}}{\partial \boldsymbol{r}_i} \right], \tag{2.8}$$

$$\frac{\partial E}{\partial \boldsymbol{r}_j} = \sum_{i} \left[\frac{dV_R(r_{ij})}{dr_{ij}} \frac{\partial r_{ij}}{\partial \boldsymbol{r}_j} - \overline{B}_{ij} \frac{dV_A(r_{ij})}{dr_{ij}} \frac{\partial r_{ij}}{\partial \boldsymbol{r}_j} - V_A(r_{ij}) \frac{\partial \overline{B}_{ij}}{\partial \boldsymbol{r}_j} \right], \tag{2.9}$$

$$\frac{\partial E}{\partial \boldsymbol{r}_k} = \sum_{i} \sum_{j>i} \left[-V_A(r_{ij}) \frac{\partial \overline{B}_{ij}}{\partial \boldsymbol{r}_k} \right], \tag{2.10}$$

$$\frac{dV_R}{dr} = \frac{df_{ij}}{dr} \frac{D}{S-1} \exp\left[-\sqrt{2S}\beta(r-R) \right] + V_R(r)(-\sqrt{2S}\beta), \tag{2.11}$$

$$\frac{dV_A}{dr} = \frac{df_{ij}}{dr} \frac{DS}{S-1} \exp\left[-\sqrt{\frac{2}{S}}\beta(r-R) \right] + V_A(r)(-\sqrt{\frac{2}{S}}\beta), \tag{2.12}$$

$$\frac{df_{ij}}{dr} = \begin{cases} 0, & r \le R^{(1)} \\ -\frac{1}{2}\frac{\pi}{R^{(2)}-R^{(1)}} \sin\left[\pi \frac{(r-R^{(1)})}{R^{(2)}-R^{(1)}} \right], & R^{(1)} < r < R^{(2)} \\ 0, & r \ge R^{(2)} \end{cases}, \tag{2.13}$$

$$T_{ij} = 1 + \sum_{k \ne i,j} G(\theta_{ijk}) f_{ik}(r_{ik}) \exp\left\{ \alpha[(r_{ij}-R) - (r_{ik}-R)] \right\}, \tag{2.14}$$

$$T_{ji} = 1 + \sum_{k \ne i,j} G(\theta_{jik}) f_{jk}(r_{jk}) \exp\left\{ \alpha[(r_{ij}-R) - (r_{jk}-R)] \right\}, \tag{2.15}$$

$$\frac{\partial \overline{B}_{ij}}{\partial \boldsymbol{r}_i} = \frac{1}{2} \left[\frac{\partial B_{ij}}{\partial \boldsymbol{r}_i} + \frac{\partial B_{ji}}{\partial \boldsymbol{r}_i} \right], \tag{2.16}$$

$$\frac{\partial B_{ij}}{\partial \boldsymbol{r}_i} = (-\delta) \frac{B_{ij}}{T_{ij}} \frac{\partial T_{ij}}{\partial \boldsymbol{r}_i}, \tag{2.17}$$

$$\frac{\partial T_{ij}}{\partial \boldsymbol{r}_i} = \frac{\partial T_{ij}}{\partial \cos\theta_{ijk}} \frac{\partial \cos\theta_{ijk}}{\partial \boldsymbol{r}_i} + \frac{\partial T_{ij}}{\partial r_{ij}} \frac{\partial r_{ij}}{\partial \boldsymbol{r}_i} + \frac{\partial T_{ij}}{\partial r_{ik}} \frac{\partial r_{ik}}{\partial \boldsymbol{r}_i}, \tag{2.18}$$

$$\frac{\partial T_{ij}}{\partial \cos\theta} = \sum_{k\neq i,j} \frac{\partial G}{\partial \cos\theta} f_{ik}(r_{ik}) \exp\left\{\alpha[(r_{ij}-R)-(r_{ik}-R)]\right\}, \tag{2.19}$$

$$\frac{\partial G}{\partial \cos\theta} = \frac{\alpha_0 c_0^2 2(1+\cos\theta)}{[d_0^2+(1+\cos\theta)^2]^2}, \tag{2.20}$$

$$\frac{\partial T_{ij}}{\partial r_{ij}} = \sum_{k\neq i,j} G(\theta_{ijk}) f_{ik}(r_{ik}) \alpha \exp\left\{\alpha[(r_{ij}-R)-(r_{ik}-R)]\right\}, \tag{2.21}$$

$$\frac{\partial T_{ij}}{\partial r_{ik}} = \sum_{k\neq i,j} G(\theta_{ijk}) \left(\frac{df_{ik}}{dr_{ik}} - f_{ik}\alpha\right) \times \exp\left\{\alpha[(r_{ij}-R)-(r_{ik}-R)]\right\}, \tag{2.22}$$

$$\frac{\partial B_{ji}}{\partial \boldsymbol{r}_i} = (-\delta)\frac{B_{ji}}{T_{ji}} \frac{\partial T_{ji}}{\partial \boldsymbol{r}_i}, \tag{2.23}$$

$$\frac{\partial T_{ji}}{\partial \boldsymbol{r}_i} = \frac{\partial T_{ji}}{\partial \cos\theta_{jik}} \frac{\partial \cos\theta_{jik}}{\partial \boldsymbol{r}_i} + \frac{\partial T_{ji}}{\partial r_{ij}} \frac{\partial r_{ij}}{\partial \boldsymbol{r}_i}, \tag{2.24}$$

$$\frac{\partial T_{ji}}{\partial \cos\theta} = \sum_{k\neq i,j} \frac{\partial G}{\partial \cos\theta} f_{jk}(r_{jk}) \exp\left\{\alpha[(r_{ij}-R)-(r_{jk}-R)]\right\}, \tag{2.25}$$

$$\frac{\partial T_{ji}}{\partial r_{ij}} = \sum_{k\neq i,j} G(\theta_{jik}) f_{jk}(r_{jk}) \alpha \exp\left\{\alpha[(r_{ij}-R)-(r_{jk}-R)]\right\}, \tag{2.26}$$

$$\frac{\partial T_{ji}}{\partial r_{jk}} = \sum_{k\neq i,j} G(\theta_{jik}) \left(\frac{df_{jk}}{dr_{jk}} - f_{jk}\alpha\right) \times \exp\left\{\alpha[(r_{ij}-R)-(r_{jk}-R)]\right\}, \tag{2.27}$$

$$\frac{\partial \bar{B}_{ij}}{\partial \boldsymbol{r}_j} = \frac{1}{2}\left[\frac{\partial B_{ij}}{\partial \boldsymbol{r}_j} + \frac{\partial B_{ji}}{\partial \boldsymbol{r}_j}\right], \tag{2.28}$$

$$\frac{\partial B_{ij}}{\partial \boldsymbol{r}_j} = (-\delta)\frac{B_{ij}}{T_{ij}} \frac{\partial T_{ij}}{\partial \boldsymbol{r}_j}, \tag{2.29}$$

$$\frac{\partial T_{ij}}{\partial \boldsymbol{r}_j} = \frac{\partial T_{ij}}{\partial \cos\theta_{ijk}} \frac{\partial \cos\theta_{ijk}}{\partial \boldsymbol{r}_j} + \frac{\partial T_{ij}}{\partial r_{ij}} \frac{\partial r_{ij}}{\partial \boldsymbol{r}_j}, \tag{2.30}$$

$$\frac{\partial B_{ji}}{\partial \boldsymbol{r}_j} = (-\delta)\frac{B_{ji}}{T_{ji}} \frac{\partial T_{ji}}{\partial \boldsymbol{r}_j}, \tag{2.31}$$

$$\frac{\partial T_{ji}}{\partial \boldsymbol{r}_j} = \frac{\partial T_{ji}}{\partial \cos\theta_{jik}} \frac{\partial \cos\theta_{jik}}{\partial \boldsymbol{r}_j} + \frac{\partial T_{ji}}{\partial r_{ij}} \frac{\partial r_{ij}}{\partial \boldsymbol{r}_j} + \frac{\partial T_{ji}}{\partial r_{jk}} \frac{\partial r_{jk}}{\partial \boldsymbol{r}_j}, \tag{2.32}$$

$$\frac{\partial \bar{B}_{ij}}{\partial \boldsymbol{r}_k} = \frac{1}{2}\left[\frac{\partial B_{ij}}{\partial \boldsymbol{r}_k} + \frac{\partial B_{ji}}{\partial \boldsymbol{r}_k}\right], \tag{2.33}$$

$$\frac{\partial B_{ij}}{\partial \boldsymbol{r}_k} = (-\delta)\frac{B_{ij}}{T_{ij}} \frac{\partial T_{ij}}{\partial \boldsymbol{r}_k}, \tag{2.34}$$

$$\frac{\partial T_{ij}}{\partial \boldsymbol{r}_k} = \frac{\partial T_{ij}}{\partial \cos\theta_{ijk}} \frac{\partial \cos\theta_{ijk}}{\partial \boldsymbol{r}_k} + \frac{\partial T_{ij}}{\partial r_{ik}} \frac{\partial r_{ik}}{\partial \boldsymbol{r}_k}, \tag{2.35}$$

$$\frac{\partial B_{ji}}{\partial \boldsymbol{r}_k} = (-\delta) \frac{B_{ji}}{T_{ji}} \frac{\partial T_{ji}}{\partial \boldsymbol{r}_k}, \tag{2.36}$$

$$\frac{\partial T_{ji}}{\partial \boldsymbol{r}_k} = \frac{\partial T_{ji}}{\partial \cos\theta_{jik}} \frac{\partial \cos\theta_{jik}}{\partial \boldsymbol{r}_k} + \frac{\partial T_{ji}}{\partial r_{jk}} \frac{\partial r_{jk}}{\partial \boldsymbol{r}_k}, \tag{2.37}$$

$$\frac{\partial r_{ij}}{\partial \boldsymbol{r}_i} = \frac{\boldsymbol{r}_i - \boldsymbol{r}_j}{r_{ij}}, \tag{2.38}$$

$$\frac{\partial r_{ij}}{\partial \boldsymbol{r}_j} = -\frac{\boldsymbol{r}_i - \boldsymbol{r}_j}{r_{ij}}, \tag{2.39}$$

$$\frac{\partial r_{ik}}{\partial \boldsymbol{r}_i} = \frac{\boldsymbol{r}_i - \boldsymbol{r}_k}{r_{ik}}, \tag{2.40}$$

$$\frac{\partial r_{ik}}{\partial \boldsymbol{r}_k} = -\frac{\boldsymbol{r}_i - \boldsymbol{r}_k}{r_{ik}}, \tag{2.41}$$

$$\frac{\partial r_{jk}}{\partial \boldsymbol{r}_j} = \frac{\boldsymbol{r}_j - \boldsymbol{r}_k}{r_{jk}}, \tag{2.42}$$

$$\frac{\partial r_{jk}}{\partial \boldsymbol{r}_k} = -\frac{\boldsymbol{r}_j - \boldsymbol{r}_k}{r_{jk}}, \tag{2.43}$$

$$\begin{aligned} \frac{\partial \cos\theta_{ijk}}{\partial \boldsymbol{r}_i} = {} & \frac{1}{r_{ij}} \left(\frac{\partial r_{ik}}{\partial \boldsymbol{r}_i} - \cos\theta_{ijk} \frac{\partial r_{ij}}{\partial \boldsymbol{r}_i} \right), \\ & + \frac{1}{r_{ik}} \left(\frac{\partial r_{ij}}{\partial \boldsymbol{r}_i} - \cos\theta_{ijk} \frac{\partial r_{ik}}{\partial \boldsymbol{r}_i} \right), \end{aligned} \tag{2.44}$$

$$\frac{\partial \cos\theta_{ijk}}{\partial \boldsymbol{r}_j} = -\frac{1}{r_{ij}} \left(\frac{\partial r_{ik}}{\partial \boldsymbol{r}_i} - \cos\theta_{ijk} \frac{\partial r_{ij}}{\partial \boldsymbol{r}_i} \right), \tag{2.45}$$

$$\frac{\partial \cos\theta_{ijk}}{\partial \boldsymbol{r}_k} = -\frac{1}{r_{ik}} \left(\frac{\partial r_{ij}}{\partial \boldsymbol{r}_i} - \cos\theta_{ijk} \frac{\partial r_{ik}}{\partial \boldsymbol{r}_i} \right), \tag{2.46}$$

$$\frac{\partial \cos\theta_{jik}}{\partial \boldsymbol{r}_i} = -\frac{1}{r_{ij}} \left(\frac{\partial r_{jk}}{\partial \boldsymbol{r}_j} + \cos\theta_{jik} \frac{\partial r_{ij}}{\partial \boldsymbol{r}_i} \right), \tag{2.47}$$

$$\begin{aligned} \frac{\partial \cos\theta_{jik}}{\partial \boldsymbol{r}_j} = {} & \frac{1}{r_{ij}} \left(\frac{\partial r_{jk}}{\partial \boldsymbol{r}_j} + \cos\theta_{jik} \frac{\partial r_{ij}}{\partial \boldsymbol{r}_i} \right) \\ & + \frac{1}{r_{jk}} \left(-\frac{\partial r_{ij}}{\partial \boldsymbol{r}_i} - \cos\theta_{jik} \frac{\partial r_{jk}}{\partial \boldsymbol{r}_j} \right), \end{aligned} \tag{2.48}$$

$$\frac{\partial \cos\theta_{jik}}{\partial \boldsymbol{r}_k} = -\frac{1}{r_{jk}} \left(-\frac{\partial r_{ij}}{\partial \boldsymbol{r}_i} - \cos\theta_{jik} \frac{\partial r_{jk}}{\partial \boldsymbol{r}_j} \right). \tag{2.49}$$

2.1.3 Model potential for inter-layer of carbons

In the Brenner-type potential, the cut-off distance of the interaction is 2.0 Å. It means that only the interaction between the nearest neighbor atoms belonging to the same layer is considered for graphite, since the inter-layer

distance of graphite is about 3.35Å. To take into account the inter-layer interaction of graphite, we construct the following interatomic potential model for the dispersion (or the van der Waals) forces between the C atoms in mutually different layers to add it to the CL potential:

$$V_{\mathrm{vdw}}(r) = 4\varepsilon\left\{\left(\frac{\sigma}{r}\right)^{12} - g(Z)\left(\frac{\sigma}{r}\right)^{6}\right\} f(r), \tag{2.50}$$

$$\varepsilon = 2.84\mathrm{meV}, \tag{2.51}$$

$$\sigma = 3.35\text{Å}, \tag{2.52}$$

$$g(Z) = (0.98 + 0.07h(Z))^6, \tag{2.53}$$

$$h(Z) = \frac{1}{\exp((Z-7)/0.05)+1}, \tag{2.54}$$

$$f(r) = \begin{cases} 1 & r < a_1 \\ \frac{1}{2}\left(1+\cos\left(\pi\frac{r-a_1}{a_2-a_1}\right)\right) & a_1 \le r \le a_2 \\ 0 & a_2 < r \end{cases}, \tag{2.55}$$

$$a_1 = 5.4\text{Å}, \tag{2.56}$$

$$a_2 = 5.8\text{Å}, \tag{2.57}$$

with the distance r between the C atoms belonging to different layers. The basic form of $V_{\mathrm{vdW}}(r)$ is the Lennard-Jones potential. The function $f(r)$ works to cut-off the potential becoming zero gradually at a long distance. The function $g(Z)$ changes relating to the degree of similarity to the AA-sequence of the graphite with the coordination number Z of atoms in a neighboring layer for a given atom. The parameters $\varepsilon = 2.84$ meV and $\sigma = 3.35$ Å are set in order to reproduce the experimental inter-layer energy and distance of the graphite, respectively.

Parameter Z is decided in the following procedures. Firstly a certain atom i is projected to the upper (or lower) layer and the projected distance x_{ik} is measured for each atom k in the projected layer. The relations of the projected distance x_{ik} and the integration of coordination number for some layered structures are shown in Fig. 2.1.

From Fig. 2.1, integrated coordination number becomes maximum for AA-sequence structure and minimum for AB-one when projected distance x_{ik} is in the range of $2.59\text{Å} < x_{ik} < 2.79\text{Å}$. For other layered structures, it takes value between the maximum and minimum. Therefore integrated coordination number Z_i of atom i in the range of $2.59\text{Å} < x_{ik} < 2.79\text{Å}$ is

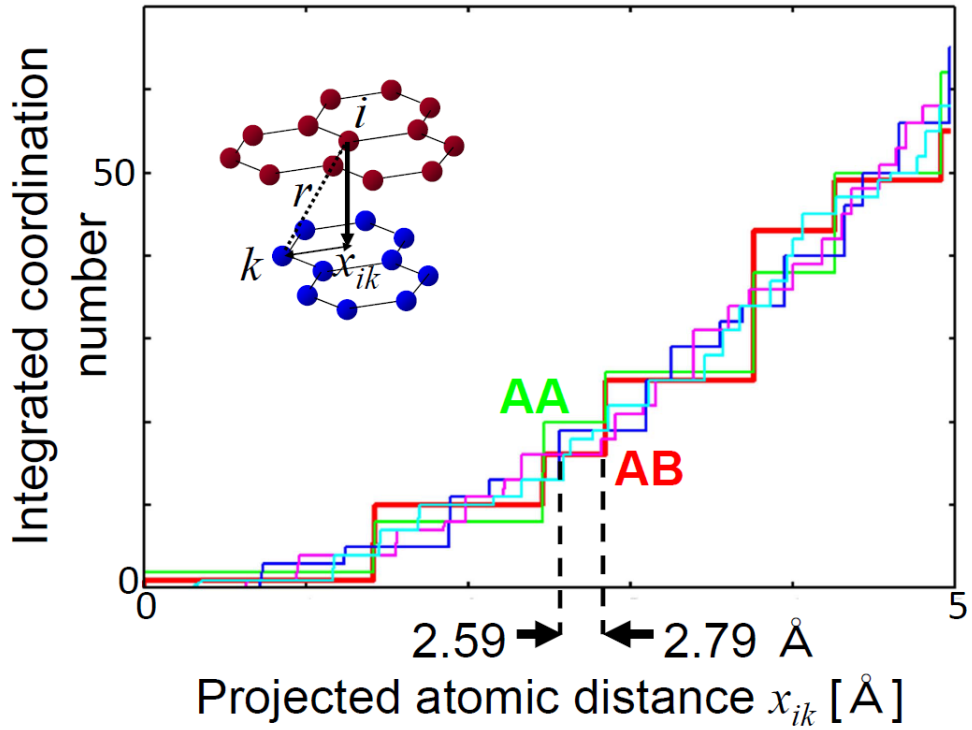

Figure 2.1: The relations of the projected distance x_{ik} and the integration of coordination number for each layered structure (AA or AB) when atom i is projected on the neighboring layer. Red, green, blue, and cyan lines correspond to AB-sequence, AA-sequence, the mid of AB- and AA- sequence structures, respectively.

obtained by the following equation:

$$Z_i = \sum_k z_{ik}, \tag{2.58}$$

$$z_{ik} = \begin{cases} 1 & x_{ik} < b_1 \\ \frac{1}{2}\left(1+\cos\left(\pi\frac{x_{ik}-b_1}{b_2-b_1}\right)\right) & b_1 \le x_{ik} \le b_2 \\ 0 & b_2 < x_{ik} \end{cases}, \tag{2.59}$$

$$b_1 = 2.59\text{Å}, \tag{2.60}$$

$$b_2 = 2.79\text{Å}. \tag{2.61}$$

Similarly, the integrated coordination number Z_j for atom j is obtained. The arithmetic mean of Z_i and Z_j provides Z:

$$Z = \frac{1}{2}(Z_i + Z_j). \tag{2.62}$$

With the CL inter-layer potential thereby constructed for C atoms, we can perform the simulation taking the inter-layer interaction of graphite into consideration.

2.2 Results and Discussion

2.2.1 Validity of intra-layer potential model of carbons

At first properties of the diamond and the graphite have been calculated in order to confirm the validity of the Brenner-type potential used in this study. The number of atom in this calculation is set to be 1728 for the diamond, 512 for the graphite. Results are shown in Table 2.2. The cohesive energy and equilibrium lattice constant computed from this simulation are good in agreement with experimental ones, but the elastic constant and bulk modulus are in disagreement. This is because the potential parameters shown in Table 2.1 are optimized to reproduce the biding energy and lattice constant of carbon materials, and it is reported that the difference with experimental value is improved when other potential parameters are used [19]. According to the purpose of the simulation, potential parameters should be determined so as to reproduce the desired properties appropriately.

2.2.2 Validity of inter-layer potential model of graphite

The primary properties related to inter-layer interaction of graphite are calculated by the CL-MD simulation to confirm the validity of the inter-layer interaction potential model settings in this study. The results are provided in Table 2.3 with experimental values. The calculated values reproduce the experimental ones with precision. Therefore the inter-layer interaction of graphite is properly considered in present model.

Table 2.2: Physical properties of diamond and graphite obtained from the CL-MD calculation with the Brenner-type potential.

		present study	experiment [20]
diamond			
lattice constant	a [Å]	3.558	3.567
cohesive energy	E_{coh} [eV/atom]	-7.346	–
elastic constant	c_{11} [GPa]	350	1081
	c_{12} [GPa]	197	125
	c_{44} [GPa]	352	579
bulk modulus	B [GPa]	248	444
graphite			
lattice constant	a [Å]	2.459	2.46
cohesive energy	E_{coh} [eV/atom]	-7.377	-7.374
elastic constant	c_{11} [GPa]	557	–
	c_{12} [GPa]	54	–
	c_{44} [GPa]	252	–
bulk modulus	B [GPa]	139	$286 - 319$

Table 2.3: Properties related to inter-layer interaction of graphite.

	present	
inter-layer distance		
(AB-type)[Å]	3.36	3.35[a]
inter-layer energy		
[meV/atom]	37.18	35[b] 52.5[c]
cohesive energy [eV/atom]		
(AB-type)	−7.41388[d]	
(AA-type)	−7.40575[d]	
energy difference		
AA−AB [meV/atom]	8.1	8[e]
phonon mode		
B_{2_g} [cm^{-1}]	134	127[f]
E_{2_g} [cm^{-1}]	34	42[f]
elastic constant		
c_{33} [GPa]	34.5	36.5[g]

a:Reference [21], *b*:Reference [22],*c*:Reference [23]
d:AB-type is more stable than AA-type in experimental
e:Reference [24], *f*:Reference [25],*g*:Reference [26]

Chapter 3

Preparatory calculations

3.1 Hybrid QM-CL simulation of diamond

The hybrid QM-CL simulation using the BCM has been applied to the diamond crystal of 1728 atoms. The simulation cell is set to be a cube 21.4Å on each side, and periodic boundary condition is adopted. When hydrogen atom is put as buffer atom, parameter β is needed in order to determine the position of the buffer atom in the QM calculation. In this study, β equals 0.72 in reference to the C-H distance 1.087Å [27] of methane (CH_4) molecules. Time step is set to be $\Delta t = 0.97$fs for the numerical integral calculus in the MD simulation. We examine a few cases of $3 \sim 29$ of atoms in the cluster region adopted the QM calculation. The crystal structure with cluster region consists of 29 atoms is indicated in Fig. 3.1.

The interatomic distance of C atoms is $1.532 \sim 1.554$ Å in the cluster region, $1.536 \sim 1.598$ Å outside the cluster region, and $1.506 \sim 1.550$ Å on the QM-CL boundary. These values are independent of setting sizes for cluster region and close to the interatomic distance of 1.545 Å estimated from each side of cell. Then, it is confirmed that crystal structure in present calculation is maintained accurately.

During a hybrid QM-CL simulation, the total energy (Hamiltonian) of system should be conserved. The time evolutions of Hamiltonian, potential energy, and kinetic energy are shown in Fig. 3.2 in the case that five atoms are selected as the cluster region for the QM calculation. Although the potential energy and kinetic energy oscillate around their equilibrium value,

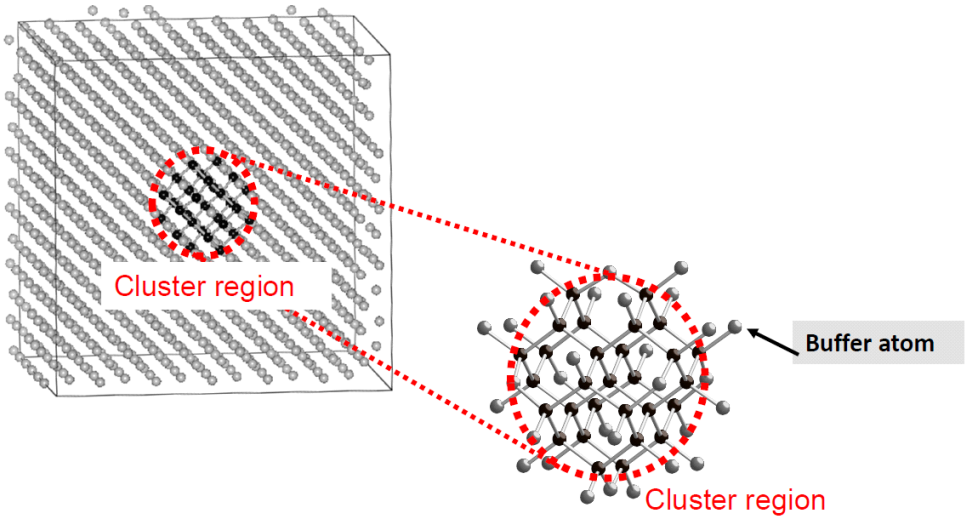

Figure 3.1: Crystal structure of diamond. Black sphere denotes the atoms adopted the QM calculation.

the Hamiltonian remains constant with a fluctuation of energy change of about 1.5×10^{-4}eV, which is converted into temperature of 1.7K. The hybrid QM-CL simulation method examined in this study is applicable definitely.

3.2 Hybrid QM-CL simulation of graphite

The hybrid QM-CL simulation using BCM is applied to the graphite composed of 320 atoms. Each side length of simulation cell is set to be $a = 17.02$Å, $b = 24.56$Å, $c = 6.70$Å, and periodic boundary condition is adopted. Twenty C atoms with brown spheres are illustrated in Fig. 3.3 as the cluster region. In addition, we also depict buffer atoms (green and peach spheres) used in the QM calculation in Fig. 3.3.

The charge density distribution in the basal plane perpendicular to the inter-layer direction (c axis) in the cluster region applied the QM calculation is shown in Fig. 3.4. The dangling bonds exist at the buffer-C atom denoted with green sphere, but charge density distribution corresponding to the dangling bonds localizes well on the buffer-C atom. Therefore, buffer atoms do not affect for the electronic structure of the central region where we want to analyze in detail. It is confirmed that the hybrid QM-CL simulation

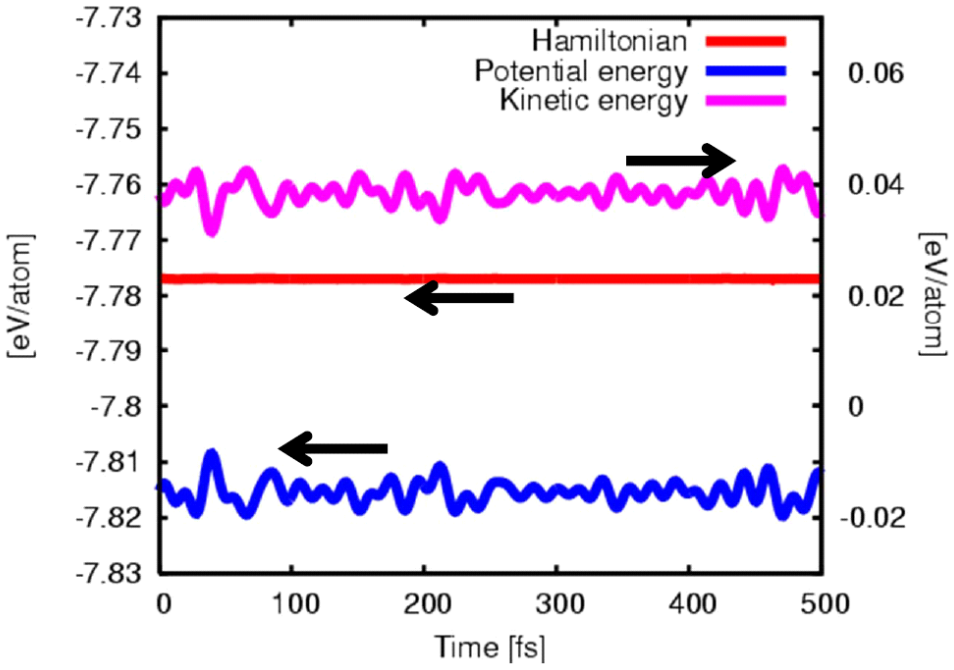

Figure 3.2: The time evolution of Hamiltonian, potential, and kinetic energy.

method using the BCM in this study gives reasonable accuracies for graphite system.

3.3 Hybrid QM-CL simulation of Li-GIC

The hybrid QM-CL simulation is applied for the Li-GIC consisting of two layers of C atoms and one Li atom. The part of graphite is composed of 240 of C atoms. Each length of cell with dimensions ($L_x = 25.52$Å,$L_y = 24.56$Å, $L_z = 7.05$Å) is prepared and periodic boundary condition is adopted. The QM-cluster region includes the inserted Li and neighboring C atoms. Typical crystal structure model of the Li-GIC in the hybrid simulation is depicted in Fig. 3.5. In the Li-GIC, AA stacking structure of C-layers is observed and we here consider AA-sequence.

We firstly set various shapes and sizes of the QM regions and check the validity and applicability of the hybrid simulation for the Li-GIC. We confirm that the crystal structure is sufficiently stable and there is no unreasonable distortion in the QM-CL boundary. Furthermore, the hybrid

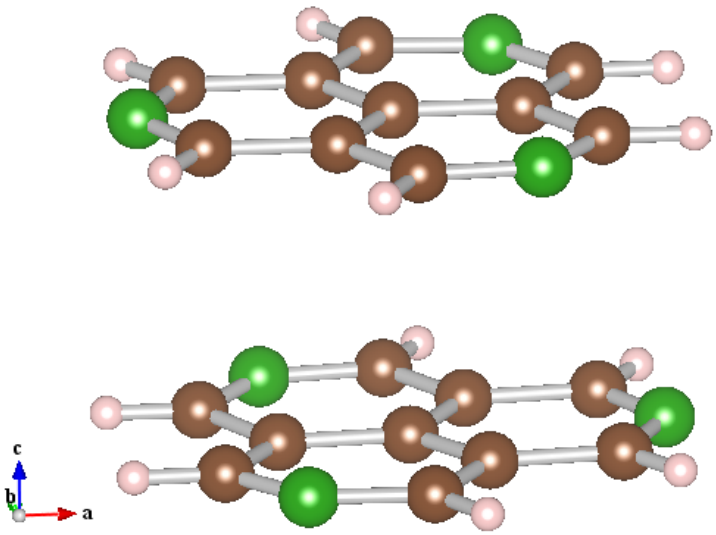

Figure 3.3: Atomic cluster model for the QM calculation of the cluster region in the hybrid QM-CL simulation for graphite. Brown, green, peach spheres depict carbon(C), buffer atom (C), and buffer atom (H), respectively.

QM-CL simulation adopted in this study gives good conservation of total energy of the QM-CL hybrid system during time evolution.

We secondary show the charge density distribution of a valence electron provided by the QM calculation in Fig. 3.6. The bonding nature between Li and C atoms which is not considered in the CL-MD calculation is able to be known by setting the QM cluster region including Li atom. In addition, since the valence electron density around the Li atom becomes almost zero, the Li has positive charge and the C atoms of graphite have negative charge as the result of charge transfer form Li to C atoms.

We will apply the hybrid QM-CL simulation method to investigate the thermal diffusion of a single Li ion in the Li-GIC. In the Li-GIC, the guest atom like the Li ion migrates with occupying certain preferential host sites. If a hybrid simulation run with the fixed selection of the QM cluster region is performed, quite large QM region and therefore huge computational times will be needed in order to trace the motion of the Li ion. To reduce the total computational time significantly, it is necessary to select adaptively

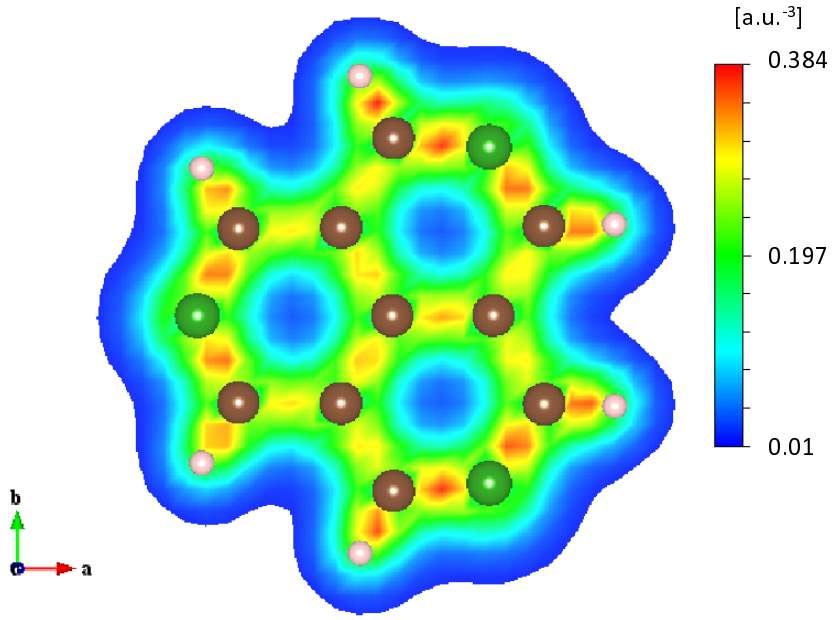

Figure 3.4: The charge density distribution in the basal plane perpendicular to the inter-layer direction (c axis) in the cluster region applied the QM calculation for graphite. Brown, green, peach spheres depict carbon(C), buffer atom (C), and buffer atom (H), respectively.

the smallest possible number of the QM atoms following the migration of the Li within acceptable physical accuracies during the simulation. Then we compare the forces acting on the Li and C atoms for various sizes of the QM cluster region in the case of the renewal of the QM region. Figure 3.7 shows the magnitude of forces for following four cases of the QM region: the small QM-region corresponds to the set of one Li and 12 C atoms expressed the red and black spheres in Fig. 3.7, the medium region is the set of one Li and 24 C atoms, the large region is the set of one Li and 48 C atoms, and the extra-large region is the set of one Li and 72 C atoms. We here note that we count total C atoms in both upper and lower layer of the Li atom before changing the cluster region. It is desirable that the forces acting on the Li and C atoms hardly vary before and after changing of the cluster region. From Fig. 3.7, 'large' region satisfies this condition enough and it should be set as the QM cluster region in order to get rid of influence with the renewal of the QM region.

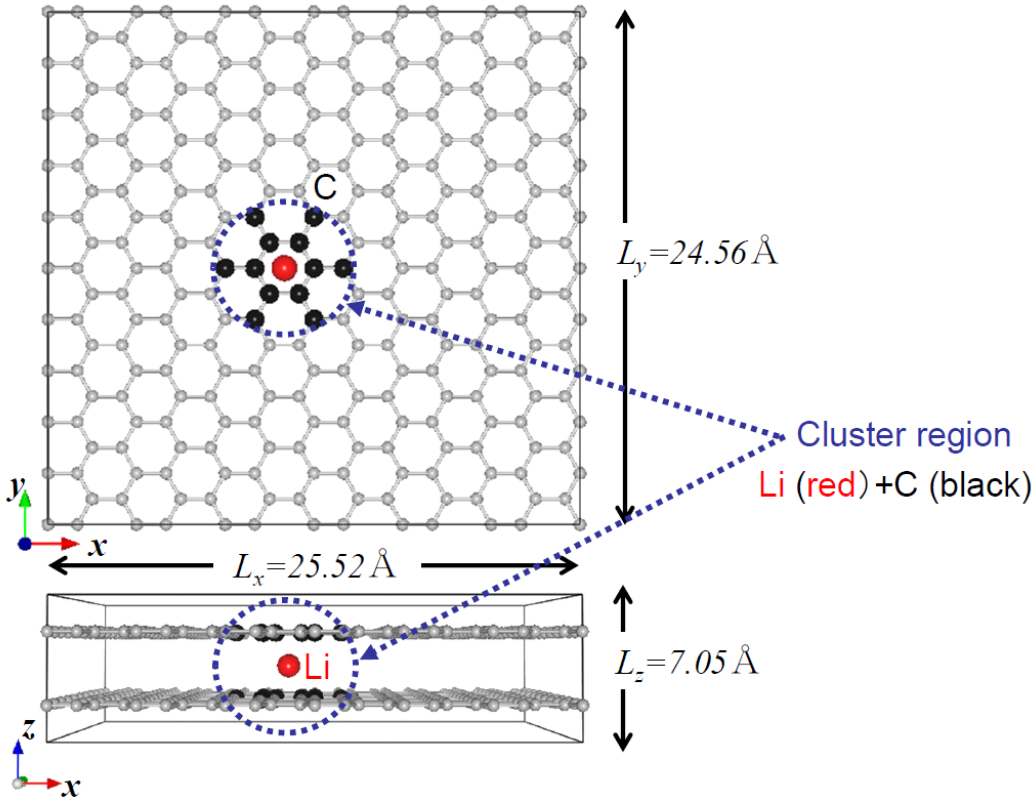

Figure 3.5: Crystal structure model of Li-GIC in the hybrid QM-CL simulation . Red (Li) and black (C) sphere depicts atoms included the QM cluster region. Gray spheres show the CL-C atoms.

A snapshot of the Li diffusion process provided from a hybrid calculation is depicted in Fig. 3.8. The upper and lower C-layers of the inserted Li are set to be AA-stacking structure, and other C-layers are set to be AB-one. The motion of Li atom at temperature of $T = 398$ K is tempted by that of the graphite C atoms, and tends to become slow when the movement of the C atoms calms down. The mean square displacement in respect to time t is shown in Fig. 3.9. The diffusion coefficient calculated from the mean-square-displacement of Li atom in the present hybrid dynamics is estimated as 7×10^{-5}cm^2/sec, which is in good agreement with experimental one reported values of order of 10^{-5}cm^2/sec for the dilute Li density phase [28]. If the inter-layer interaction of graphite is not considered, the calculated diffusion coefficient is ten times larger than that with the

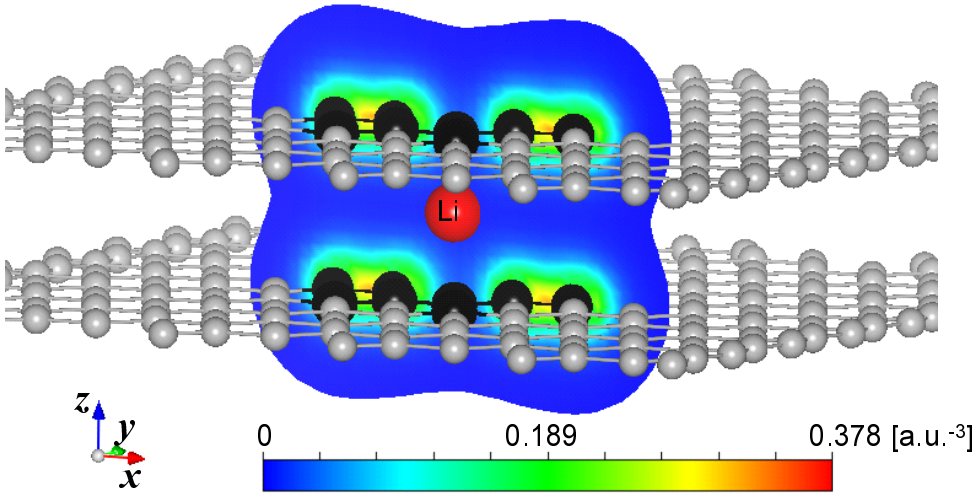

Figure 3.6: The valence charge-density distribution around the Li atom in (0100) plane. The large red, gray and small black spheres indicate Li, C and quantum-calculated C atoms, respectively.

inter-layer interaction. The effect of the inter-layer interaction is important for the diffusion process of the Li in the Li-GIC.

The stacking structure of the graphite is AB sequence generally, but it is known to change into AA-type by the insertion of Li. Therefore, at temperature $T = 398K$, we examine a Li diffusion process while stacking structure of the C-layers are varying with AB $\Leftrightarrow$ AA, assuming the following procedures:

- A Li atom is inserted to AB sequence type of graphite.
- Very small force, which hardly influence on temperature, is provided to the upper layer of the inserted Li and then stacking structure of layers sandwiching Li changes to AA sequence.
- Dynamics is investigated with varying the number of Li atom. (Li is set 1 or 2 for 1728 of C atoms.)

The time evolution of parameter Z which distinguishes AB-type sequence from AA-type of the C-layers and trajectory of Li are shown in Fig. 3.10. Parameter Z becomes 8 for AB-type structure, on while 10 for AA-type. It takes between 8 and 10 for the intermediate structure of AA- and AB-type. When Li density is dilute like this calculation condition, the

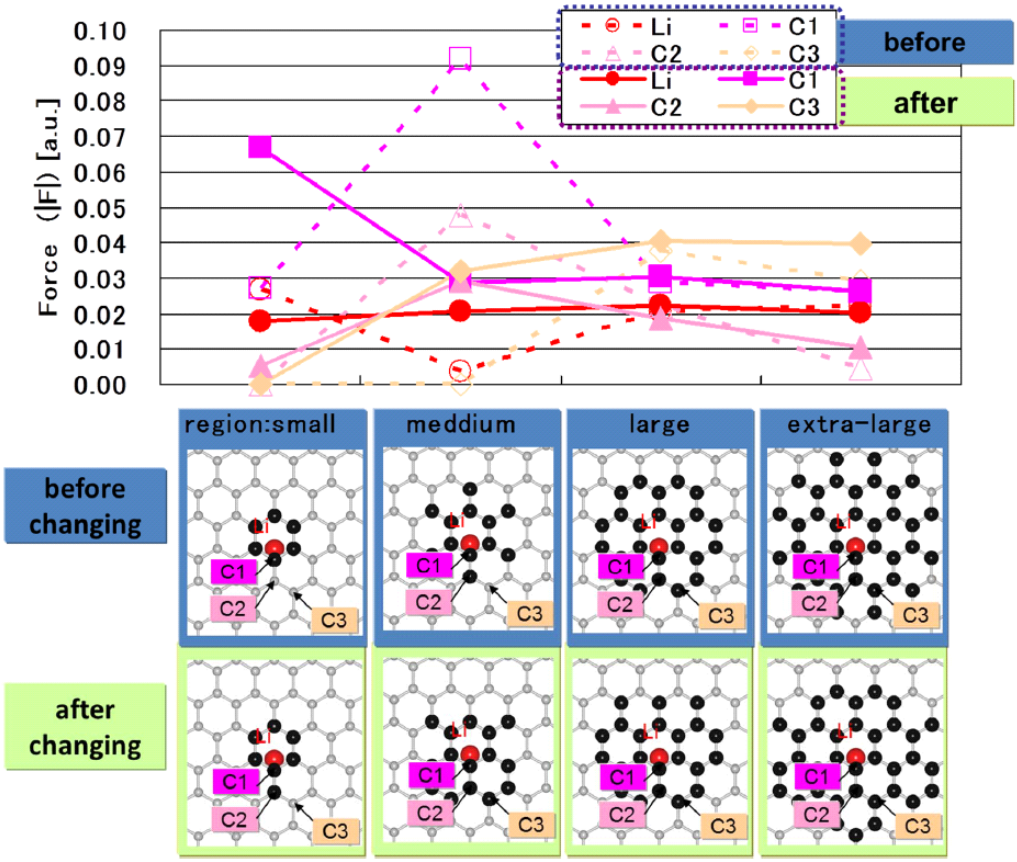

Figure 3.7: Before and after the change of the cluster region, the forces acting Li and C atoms around it. Red (Li) and black (C) sphere depicts atoms included the cluster region.

stacking structure of C-layers once changes into AA sequence by the Li insertion, however, it changes into AB sequence immediately. Therefore it is thought that the C-layers of the Li-GIC have AB-type structure in the initial stage of Li insertion. On the other hand, the case of higher Li density can keep AA-type structure longer than AB-type. So, the C-layers in the Li-GIC become AA sequence with increasing the Li density. In addition, trajectories of Li suggest that Li moves well in varying from AA- to AB-type sequence.

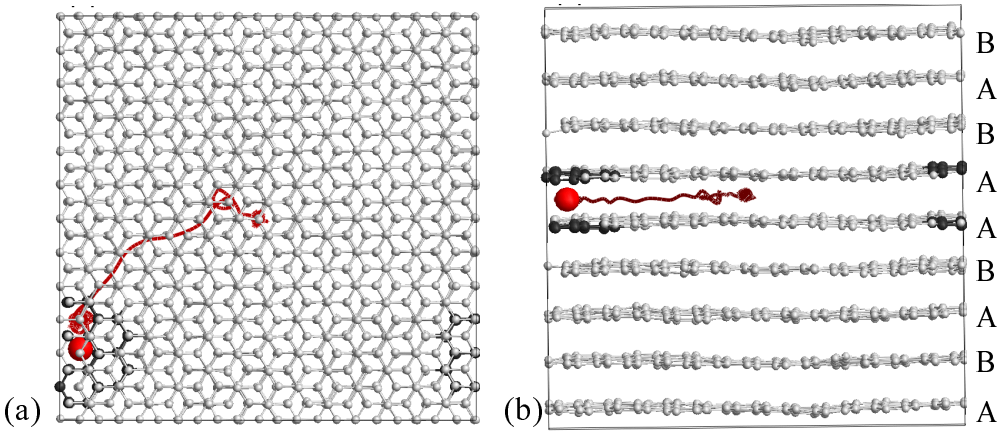

Figure 3.8: A snapshot of Li diffusion process provided from a hybrid calculation at temperature of $T = 398$ K. Red, black, and white spheres are Li, QM-calculated C, and CL-calculated C atoms, respectively. Trajectory of Li is also drawn. (a)Top view. (b)Side view. The letters of "A" or "B" denote the stacking structure of C-layers.

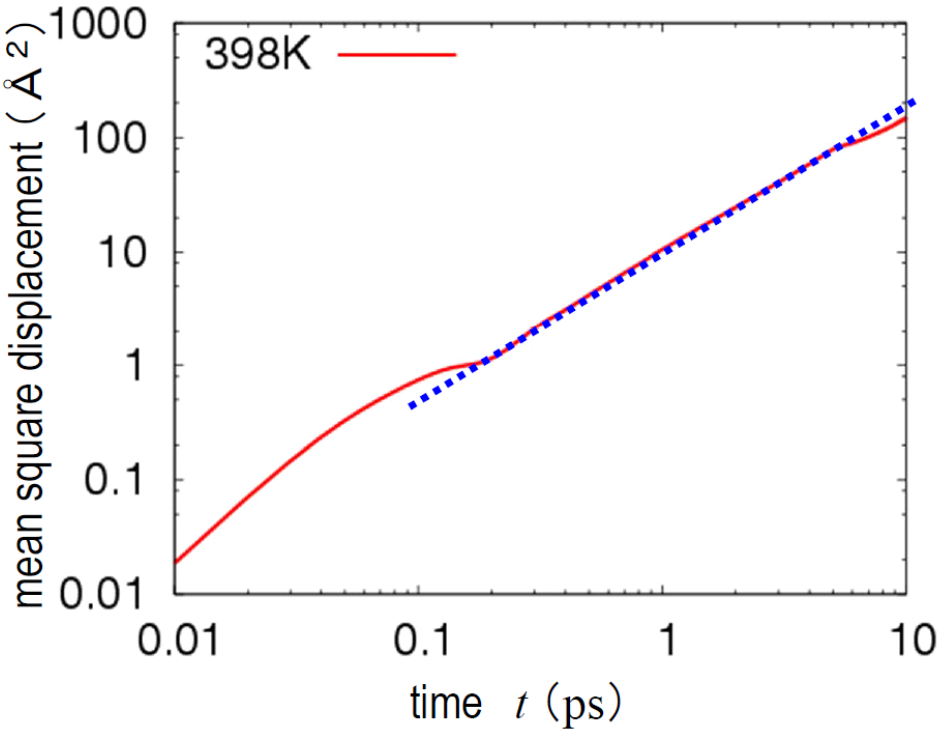

Figure 3.9: Time evolution of mean square displacements of Li at temperature $T = 398K$. Dot straight line shows the line approximated for the calculation of the diffusion coefficient.

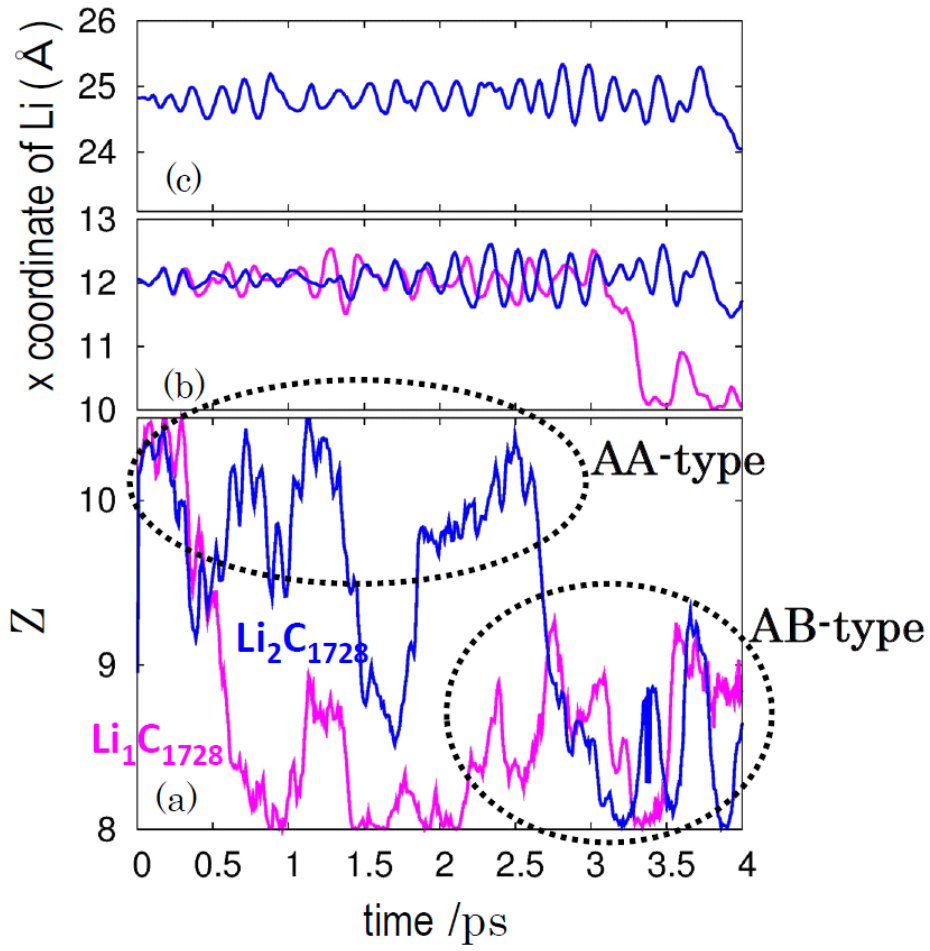

Figure 3.10: (a)The time evolution of parameter Z which distinguishes AB-type from AA of the C layers in Li-GIC. (b,c)Trajectories of x coordinate of Li. Blue (magenta) line depicts in the case of one (two) Li atom(s).

Chapter 4

Stress-dependence of Li diffusivity in graphite

4.1 Introduction

The graphite can form various intercalation compounds by incorporating atoms (ions) and small molecules between its layers. The lithium (Li)-graphite intercalation compound (Li-GIC) is put to practical use as a negative electrode of the Li-ion rechargeable battery. In the battery, the Li ions are shuttled between the positive and negative electrodes by the applied voltage through the nonaqueous electrolyte and separator. Such charge-discharge reactions in the Li-ion battery involve following key processes: the transport of the Li ions in both electrode and electrolyte materials, the charge transfer at the electrolyte-electrode interfaces, and the internal structural changes of the electrodes as the Li density is increased. Much interest exists to advance the power, capacity, and durability of the Li-ion battery relating to the recent electric power saving and environmental problems. Among the key processes, the transport process of the Li ions in the graphite layers is related directly to the power performance of the Li-ion batteries. We will address the problem of the Li diffusivity in the graphite at finite temperatures by exploiting the concurrent-type hybrid simulation technique developed recently. Our investigation of the Li diffusivity in the graphite is not only interesting as a fundamental physical process but also important to design advanced Li-ion batteries.

It is well known that the inter-layer distance of the Li-GIC expands by about 10% with the insertion of the Li: for instance, the distance is 3.35 Å for pure graphite, while 3.70 Å for LiC_6 [29]. We here note that the Li-GIC transforms among various microscopic structures [30] accompanied with the change in the layer-stacking sequence as the averaged Li-density increases: the random-stage structure is seen at low Li-density, the stage-4 structure that denotes the existence of four C-layers between the inserted Li-layers at a higher Li-density, the stage-3 structure at a much higher Li-density, etc.; the AB sequence at low Li-density, while the AA sequence at high Li-density as in LiC_6. Owing to the high stiffness of the C-layer in parallel to the layer surface, those structural and sequential changes of the Li-GIC should extend to the long range. The expansion around the Li ion mentioned above creates the stress field in the C layers, which should affect the Li diffusivity. The relation between the Li diffusivity and the stress field is expected also for the following situation. Since the layers of the graphite are easy to be compressed or stretched due to their weak C-C interaction through the dispersion force, it is natural to expect that the Li ion may diffuse slower or faster when the graphite is pushed or pulled, respectively. Despite the fundamental importance of the issue, no quantitative evidences have been reported about the possible stress (or inter-layer distance) dependence of the Li diffusivity either from experiments or simulations.

Motivated by those, in the present paper, we will investigate the relation between the Li diffusivity and inter-layer distance of the graphite by the hybrid quantum (QM)-classical (CL) simulation method [31, 15, 32]. The hybrid QM-CL simulation method has been attracting great attention as it is one of the methods that aim to treat large-scale atomistic system with high physical accuracies. In the hybrid method, the QM region whose electronic structures are calculated explicitly by the first-principles method as the density-functional theory (DFT) is embedded in a CL system of atoms that uses an empirical interatomic potential model. In the present study, we consider a single Li-ion inserted in the graphite; the total system is charge neutral. The QM region that includes the inserted Li and neighboring C atoms is treated by the DFT implemented in real space. The CL method that uses an empirical interatomic potential is applied to the rest of the

graphite. The buffered cluster method [3] is adopted to couple the QM and CL regions dynamically.

Remarkable merits of using the hybrid QM-CL method for the present simulation of the Li ion in the graphite are the following. (i) The hybrid QM-CL method can investigate the diffusion process of the Li-GIC with the influence of surrounding C atoms taken into consideration at a reasonable computational cost. On the other hand, the CL molecular dynamics (MD) method cannot describe generally the chemical reactions such as the charge transfer between the Li and C atoms. Also the first-principles MD method that uses the DFT for electronic structure calculation cannot treat a large-scale graphite system required to study the migration of the Li ion. (ii) The dispersion forces for the inter-layer interaction of the graphite can be incorporated easily through the CL interatomic potential model in the hybrid QM-CL method. Remember that the dispersion force cannot be taken into consideration in the conventional DFT method. (iii) It is not necessary to construct an empirical interatomic potential between the Li and C atoms. If we succeed to construct the proper interatomic potential between the Li and C, we can simulate the Li diffusion in the Li-GIC by the CL-MD method. However, as we will show in § 4.3, the activation energy for the Li diffusion is quite small. It is not easy to construct a precise potential between the Li and C atoms for our purposes.

The rest of the present paper is organized as follows. In § 4.2, we will describe briefly the simulation method and system. Section 4.3 will report the simulation results on the Li dynamics in the graphite at various settings. We will discuss about the relation between the inter-layer distance and the Li diffusivity. Possible explanation for the significant lowering of the Li diffusivity observed experimentally at the situation of mixed stage-structures will be given. We will conclude the present study in § 4.4.

4.2 Hybrid QM-CL simulation method

We apply the hybrid QM-CL simulation method to investigate the thermal diffusion of a single Li-ion in the graphite with both compression and stretching of the averaged inter-layer distance of the graphite. The details of

the hybrid QM-CL simulation method can be found in Refs. [3, 18, 32].

4.2.1 Buffered cluster method

In the hybrid QM-CL simulation method, a cluster of atoms is selected from the total system as the QM region. The Li ion and its surrounding C atoms make the QM region in the present simulation. Artificial dangling bonds therefore form at the QM-CL boundary. Possible influence of the dangling bonds on the electronic states and the atomic forces should be minimized. The link-atom method that uses the hydrogen atoms for termination of the dangling bonds is often adopted to couple the QM and CL regions. Depending on the selection of the QM region, however, using the link atom method results in significant relaxation of the artificial surface of the QM region and unwanted deformation of the whole system from the original configuration. We therefore adopt the buffered cluster method (BCM) [3], which requires no link-atom and is insensitive to the selection of the QM region. To use the BCM, we put additional atoms of either H or C (i.e., constituent species), called the buffer atoms, at the QM-CL boundaries to terminate the dangling bonds. The positions of the buffer atoms are determined so as to minimize the potential energy of the corresponding cluster in classical calculation under the constraint of fixed classical buffer atoms. Note that the positions of the buffer atoms are not relaxed in the QM calculation. Thereby artificial surface relaxation of the QM region is suppressed in the BCM.

4.2.2 QM calculation

For the QM calculation in the hybrid QM-CL simulation, we use the real-space DFT method in which the Laplacian operations in the Kohn-Sham and Poisson equations are evaluated with the finite difference method. The real-space DFT is well-suited to the present setting of the free boundary condition in the QM calculation (i.e., the atomic cluster in vacuum). The details of the algorithm were described in Refs. [31, 15, 33]. The Troullier-Martin-type normconserving pseudopotentials [34] are used to describe the interaction of the valence electrons and nuclei (ions). The

generalized gradient approximation formula introduced by Perdew, Burke, and Ernzerhof [35] is adopted to the exchange-correlation energy term. The Kohn-Sham orbitals and Hartree field are represented on the uniform Cartesian mesh points. The fourth-order finite-difference method is used for the Laplacian operation [36]. For parallel computation, those data on the mesh points are divided into domains to be stored in the compute nodes. The multi-grid method [37] is employed for acceleration of the convergence of the long-wavelength components of the data on the mesh points. The grid spacing $h = 0.45$ a.u. (1 a.u. ≈ 0.5292 Å), which corresponds to the cutoff energy $(\pi/h)^2 \approx 49$ Ry (1 Ry = 13.6 eV) in the plane waves DFT method. In addition, the smaller grid spacing of $h/3$ is used only around the atoms.

4.2.3 CL calculation

In the hybrid QM-CL simulation method, the CL-MD calculation is performed for the CL region, that is, the whole system minus the QM region. The velocity Verlet algorithm is used to integrate the Newton's equations of motion for all the atoms (or ions in the QM region). The Brenner's interatomic potential [16] is adopted for the C atoms of the graphite. We employ the parameter values listed in Table I in Ref. [16] except for the equilibrium distance. The equilibrium distance is set to 1.33116 Å so that the calculated equilibrium lattice constant of the graphite becomes equal to the one calculated with the QM calculation, which is slightly longer than that in Ref. [16]. Such a fine tuning of the parameters in the CL potential is necessary in order not to create artificial stress at the QM-CL boundary in the hybrid QM-CL simulation method [18]. In the Brenner-type potential, the cut-off distance of the interaction is 2.0 Å. It means that only the interaction between the nearest neighbor atoms belonging to the same layer is considered. To take into account the inter-layer interaction, we construct the following interatomic potential model for the dispersion (or the van der Waals) forces between the C atoms to add it to the CL potential:

$$V_{\mathrm{vdW}}(r) = 4\varepsilon \left\{ \left(\frac{\sigma}{r}\right)^{12} - g(Z) \left(\frac{\sigma}{r}\right)^{6} \right\} f(r) \tag{4.1}$$

with the distance r between the C atoms belonging to different layers. The basic form of $V_{\mathrm{vdW}}(r)$ is that of the Lennard-Jones potential. The $f(r)$ works

to cut-off the potential gradually at a long distance. The $g(Z)$ changes relating to the degree of similarity to the AA sequence of the graphite with the coordination number Z of atoms in a neighboring layer for a given atom. The parameters $\varepsilon = 2.84$ meV and $\sigma = 3.35$ Å are set in order to reproduce the experimental inter-layer energy and distance of the graphite, respectively. With the CL interatomic potential thereby constructed for C atoms, the elastic constant for the direction perpendicular to graphite layers becomes $c_{33} = 34.5$ GPa, which is in good agreement with the experimental value 36.5 GPa [26].

The hybrid QM-CL simulation will be performed in the micro-canonical ensemble, that is, the total number of atoms, the shape and volume of the simulation box, and the total energy are constant. The velocity scaling, however, will be applied to control the system temperature.

4.2.4 Target system

The simulation system is composed of 3072 C atoms and a single Li-ion under the periodic boundary condition as shown in Fig. 4.1. As will be explained in § 4.3, the charge transfer occurs between the Li and neighboring C atoms, resulting in formation of the Li^+ state. In total, eight C-layers exist. The graphite assumes the AB sequence since we are interested in the situation of low Li-density. A cluster of atoms composed of the Li and the surrounding C atoms belonging to the two sandwiching layers is set to the QM region. The dynamic selection of the C atoms around the Li ion in motion follows the rule to realize sufficient physical accuracies of the atomic forces, which is pre-determined in a way similar to Ref. [32].

To set proper sizes (L_x, L_y, L_z) of the simulation system at a finite temperature T, we begin with considering the sizes at $T = 0$ K. Here the x- and y-axes are set along the layer, while the z-axis perpendicular to the layer. The hybrid QM-CL simulation at $T = 0$ K gives $(L_x, L_y, L_z) = (34.44$ Å, 29.83 Å, 26.97 Å) as the equilibrium values. The L_x and L_y values are the same as those for the pure graphite; the L_z is only 0.1 Å longer than that for the pure graphite. Since the thermal expansion along the layer is quite small, we use the same values of (L_x, L_y) at finite temperatures also. On the other hand, the thermal expansion along the z-axis is substantial. As shown in

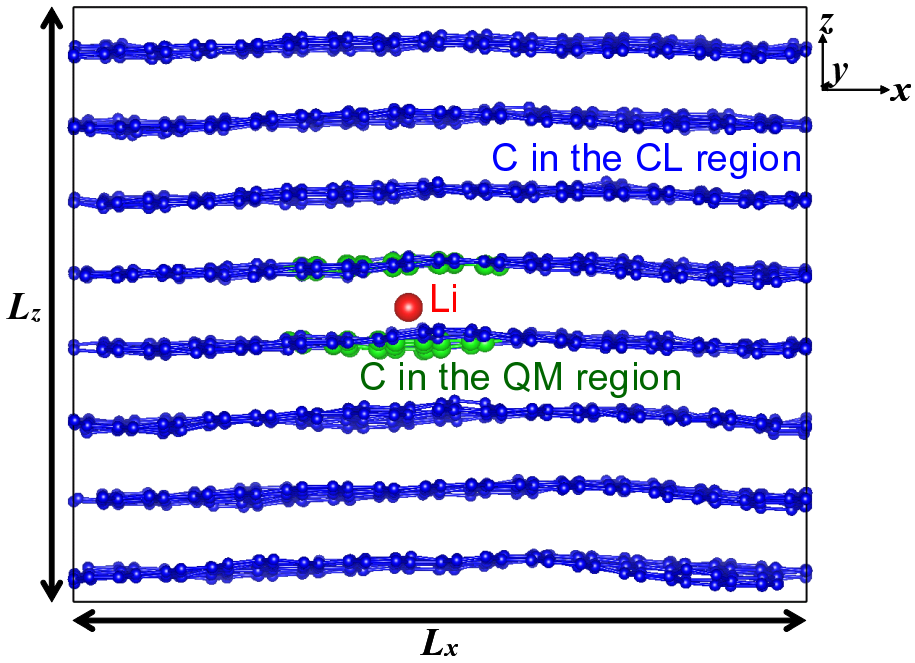

Figure 4.1: The side $(x-y)$ view of the total simulation system. The large red and medium green spheres are respectively the Li and C atoms in the QM region. The small blue spheres are the C atoms in the CL region.

Fig. 4.2, we find through separate CL-MD simulation that the coefficient of linear thermal expansion of the pure graphite in z-direction is 6.7×10^{-5} K^{-1} with the present CL potential. It is in accord with the experimental data of 7.34×10^{-5} K^{-1} [21] and is the same order with another experimental data of 2.7×10^{-5} K^{-1} [38]. We assume that the same expansion coefficient can be applied to the present system since the Li density is too small to affect the system size. Therefore, multiplying the linear expansion factor for 423 K to $L_z = 26.97$ Å for $T = 0$, we find the equilibrium value of $L_z = 27.74$ Å for $T = 423$ K.

We are interested in the possible effects of change of L_z on the Li diffusivity at $T = 423$ K. For the compressed situation, we consider -3.9% and -1.7% changes in L_z from the original value of 27.74 Å. For the stretched situation, the 2.9% change in L_z. In addition, we consider the case of 0.6% change in L_z. If we take into account the elongation of 0.35 Å in the inter-layer distance by the Li insertion [29], the resulting $L_z = 27.74 + 0.35 = 28.09$ Å may be taken as the equilibrium value at 423 K. Since $L_z = 27.92$ Å in the 0.6% case is about the middle of the two estimates (27.74 Å and 28.09 Å) for the equilibrium value of L_z at 423 K, we regard the 0.6% case as the equilibrium condition, which relates to the situation of no pressure on the layers.

4.3 Results and discussion

We depict in Fig. 4.3 the valence-electron density on a y-plane in the QM region calculated using the hybrid QM-CL simulation method. The black sphere at around the center of the QM region is the Li ion. The bonding nature between the neighboring C atoms is observed. We find almost no electrons in the vicinity of the Li, indicating significant electron transfer from Li atom to the C atoms to form the Li^+ state.

Figure 4.4 shows the mean square displacements (MSD) of the Li ion as functions of time in the four cases (-3.9%, -1.7%, 0.6%, and 2.9% changes of L_z) at $T = 423$ K. Since there exists only a single Li-ion in the system, we shift the time origin of the MSD by every 0.1 ps to increase the number of data samples for better statistics. The total simulation time is 12 ps for

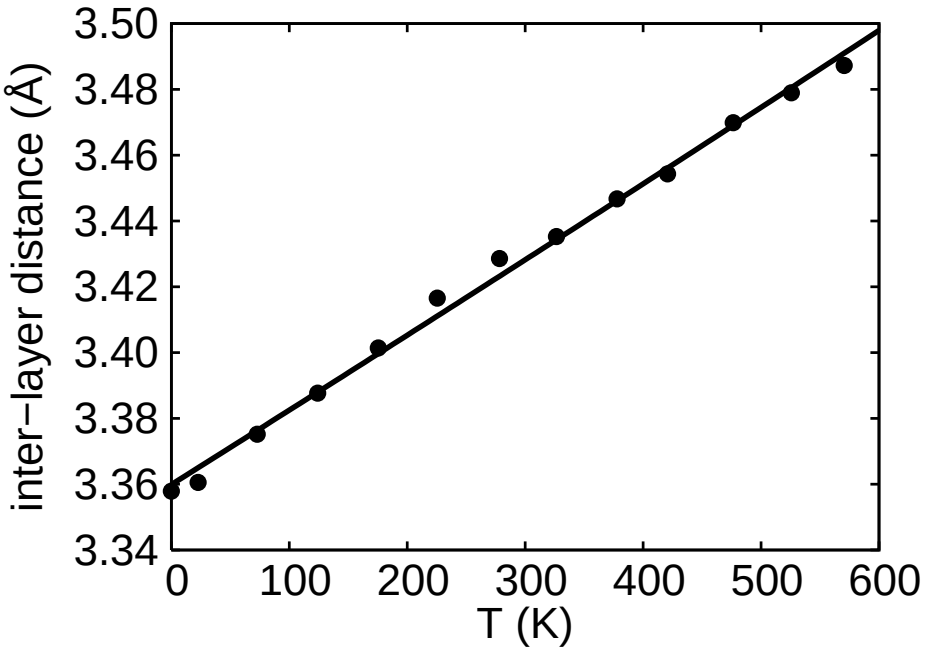

Figure 4.2: The averaged inter-layer distance of the graphite at equilibrium as a function of temperature T (K), obtained through separate classical MD simulation. The solid line shows the fitting formula $f(T) = 3.36(1 + 6.7 \times 10^{-5}T)$.

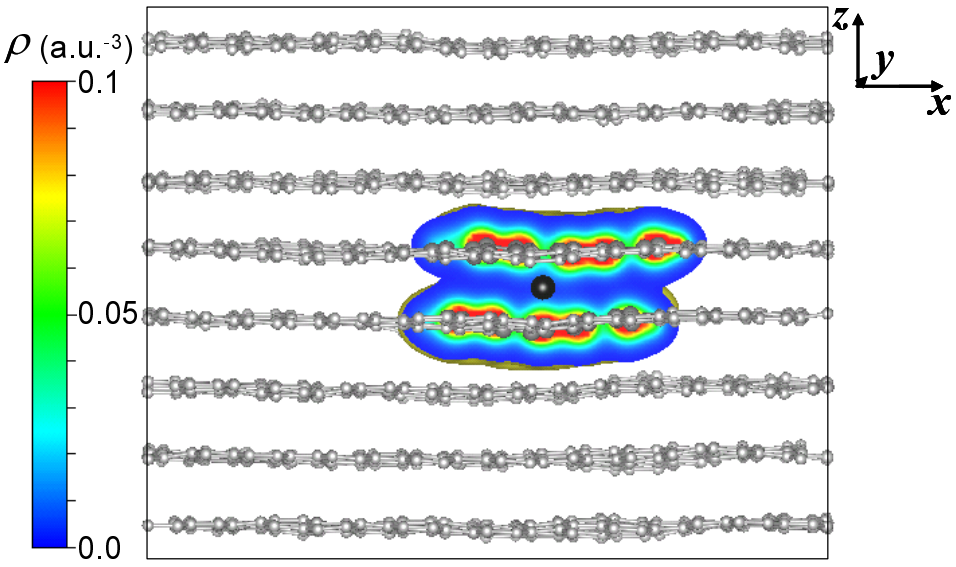

Figure 4.3: The valence-electron density on a y-plane in the QM region obtained in the hybrid QM-CL simulation. The black sphere is the Li ion, while the gray spheres the C atoms. The density less than 0.001 a.u.$^{-3}$ is omitted.

each run; the time step is 1.0 fs. Therefore the curves in Fig. 4.4 appear to have substantial fluctuations as the time (i.e., the horizontal axis) gets longer (t >4 ps). The curves in Fig. 4.4 are not linear enough to estimate the diffusion coefficients at long times. However, characteristic dependence of the Li diffusivity on the change of L_z is observed as follows.

The MSD's for $t = 0 \sim 3$ ps that have small statistical errors, show the clear dependence on L_z. As expected, the MSD's in the equilibrium (0.6%) and stretched (2.9%) cases are larger than that in the compressed (-1.7% and -3.9%) cases. In the equilibrium and stretched cases, we find a super-linear (or partly parabolic) behavior of the MSD as a function of time at short times ($t = 0 \sim 1$ ps), while a linear behavior at longer times ($t = 1 \sim 3$ ps). In the compressed cases, the MSD increases in proportion to time for $t = 0 \sim 3$ ps. The super-linear behavior in the equilibrium and stretched cases indicate a mixture of ballistic and hopping motion of the Li ion. On the other hand, the accurate linear behavior in the compressed cases means the usual hopping motion.

There exist insufficient statistics in the MSD data for $t = 4 \sim 10$ ps, resulting in large fluctuations. In the equilibrium and stretched cases, we find no obvious deviation of the MSD from the linear extrapolation of the data for $t = 1 \sim 3$ ps. In a compressed case (-1.7%), the clear change of the MSD from the linear to saturation behavior is observed. We will explain the mechanism of the saturation behavior later in this section in terms of the cage effect.

The trajectory of the Li ion during 10 ps in each run is plotted in Fig. 4.5; the initial and final positions of the Li ion are depicted with the open arrow and the large red sphere, respectively. The green spheres are the C atoms in the QM region. When the graphite layers assume the equilibrium distance or stretched one, the Li ion migrates over a wide area. On the other hand, the Li ion appears to be confined in the compressed cases, particularly in the -1.7% case. In the equilibrium and stretched cases (0.6% and 2.8%) in Fig. 4.5, we observe both hopping and ballistic modes of the Li ion motion. In the hopping mode, the Li ion moves to avoid the places at which two C atoms belonging to different layers assume the same $x - y$ positions (see, Fig. 4.6). However, as remarked in Fig.4.5 with black arrows, we find the Li

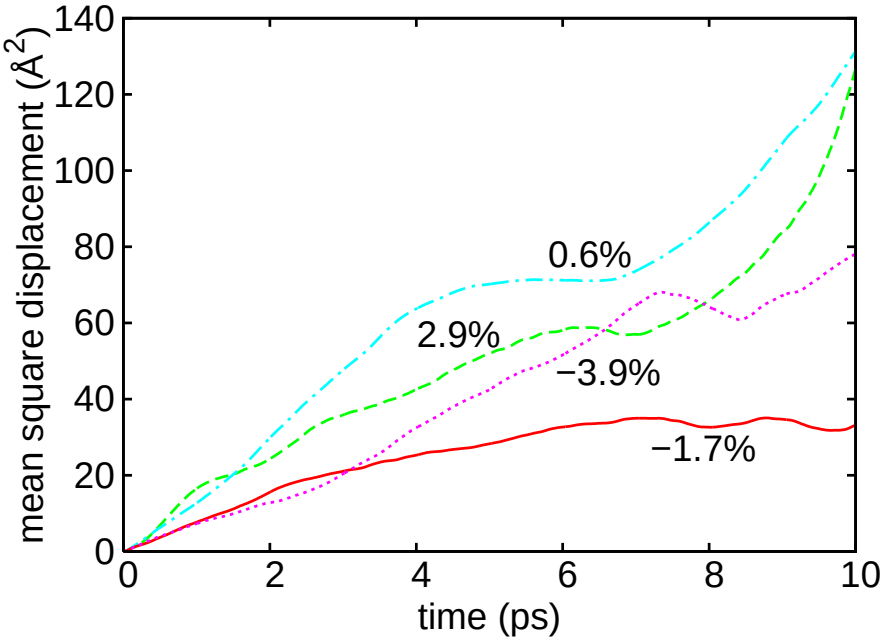

Figure 4.4: The mean square displacements of the Li ion as functions of time in the hybrid QM-CL simulation at 423 K for the compressed (-3.9% and -1.7%), equilibrium (0.6%), and stretched (2.9%) values of L_z. For better statistics, the time origins are set at every 0.1 ps in the simulation run of total 12 ps.

ion in the ballistic mode can pass through such a place. The ballistic motion makes the MSD super-linear or parabolic in time as already pointed out for the 2.9% and 0.6% cases in Fig. 4.4. Detailed analyses of the ballistic-motion events show that the inter-layer distances at near places of the Li ion toward the direction of its motion are always larger than 3.85 Å. The value 3.85 Å means stretching the inter-layer distance by 0.36 Å (0.27 Å) as compared to the averaged value in the 0.6% (2.9%) case. We, in fact, find that the thermal fluctuation produces such a local stretching frequently at various places in those simulation cases.

In order to understand the mechanisms of the Li diffusivity, the activation energy for the hopping diffusion of the Li ion is evaluated using the hybrid QM-CL simulation method. Figure 4.6 depicts the positions of the Li ion in the ground state (GS) and the transition state (TS). The activation energy, which is calculated by subtracting the energy in the GS from that in TS, in each case of the L_z change is plotted in Fig. 4.7. The activation energy obtained from the total energy, i.e., the filled sphere in Fig. 4.7, includes both contributions of the QM and CL regions. We find that the activation energy is quite small, less than 0.07 eV, irrespective of L_z. Therefore, the Li ion can diffuse easily by the thermal fluctuation. As the inter-layer distance becomes shorter, the activation energy estimated from the total energy increases substantially, which supports our finding of suppressed diffusivity by compression.

The contribution of the QM region (i.e., around the Li ion) to the activation energy changes little when the system is compressed or stretched. On the other hand, the contribution of the CL region (far from the Li ion) increases as the system is compressed, which means that the distortion of the C atoms far from the Li ion affects the activation energy. Note that the major contribution to the activation energy in compressed system comes from the CL region as seen in Fig. 4.7. Since the long-ranged distortion is formed in cooperation with a large number of C atoms, the deformation field cannot change in a short time. We guess that such a relatively long-lived deformation field works as a cage for the motion of the Li-ion, resulting in a relatively small migration area as observed clearly in the compressed case (-1.7%) in Fig. 4.5.

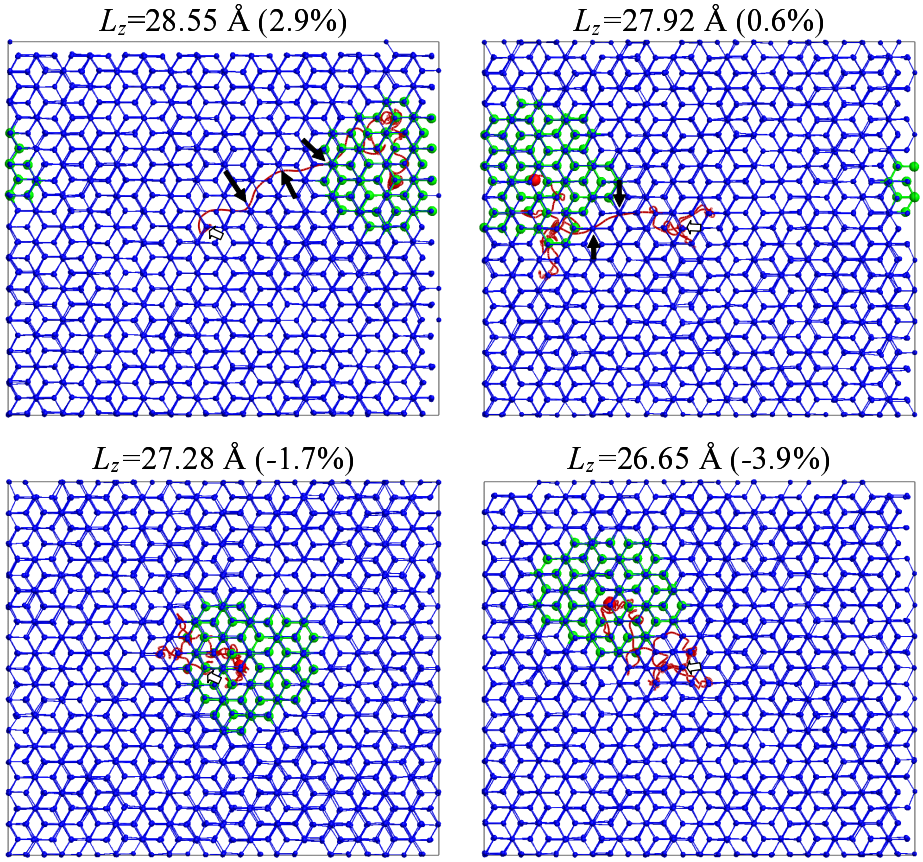

Figure 4.5: The trajectory of the Li ion during 10 ps viewed from z-direction, obtained in the hybrid QM-CL simulation. The four cases of the change of L_z are considered. The initial position of the Li ion is depicted by the open arrow. The final position by the large red sphere. The green spheres are the C atoms in the QM region. The black arrows depict the places where the Li ion passes through the places at which two C atoms belonging to different layers assume the same $x - y$ positions.

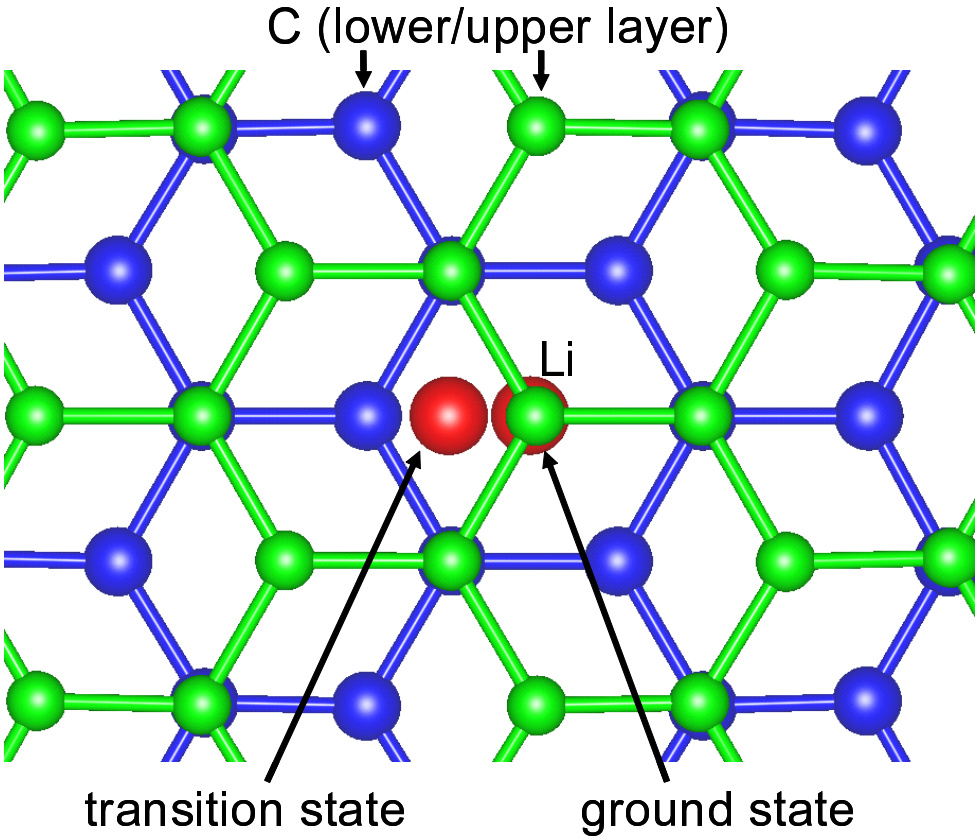

Figure 4.6: The Li ion at the ground and transition states in the hopping diffusion in the graphite. The Li ion is sandwiched by two C-layers.

The DFT calculation [39] reported that the elastic constant c_{33} of the graphite relating to the deformation perpendicular to the layers, increases with increasing the Li density. It is therefore reasonable to consider that the region around the Li ion is hard to be compressed in comparison to the one without the Li. Using the hybrid QM-CL simulation method, we calculate the local strain of the inter-layer distance at both nearby and far regions of the Li ion in the graphite at $T = 0$ K. The standard inter-layer distance at $T = 0$ K is evaluated from the equilibrium distance of the graphite system size $L_z = 26.97$ Å irrespective of regions. The local strain for a given L_z, calculated in reference to the standard value, is plotted in Fig. 4.8. The local strain at the far region changes in proportion to L_z. On the other hand, the local strain at the nearby region changes differently. The gradient of the slope with respect to L_z indicates that (i) the nearby region is harder than the pure graphite for $L_z < 26.97$ Å; (ii) it is softer for $L_z = 26.97 \sim 27.6$ Å (iii) it has similar stiffness for $L_z = 27.6 \sim 28.2$ Å. The finding (i) means the accumulation of the deformation energy in the far regions relating to its relative softness when the system is compressed. It is the reason of substantial contribution of the far region to the activation energy in the compressed situation. The similar finding of the substantial contribution of the peripheral (CL) region to the activation energy in the highly strained situation has been reported for the activation energy of the O atom in the Si crystal [18].

To analyze possible error in the activation energy, we calculate the energy with a different method in a similar setting. We use the projector augmented wave method for the DFT calculation implemented in the VASP code [40], which is expected to have higher accuracy since the core electrons are treated also in addition to the valence electrons. We prepare the supercell, $3 \times 3 \times 2$ of the unit cell, of the graphite in the AB-sequence. Then a single Li atom is inserted. Hence the total system contains 72 C atoms and 1 Li atom. The supercell and all the atomic positions are relaxed in the GS; the supercell and the positions of the C atoms in the TS. The calculated results by the VASP are listed in Table 4.1 for both GS and TS. The activation energy evaluated from the electronic energy is 0.09 eV, which is the same order of 0.05 eV obtained by the hybrid QM-CL simulation method at zero strain. Considering the difference in the target system used in the two methods, we

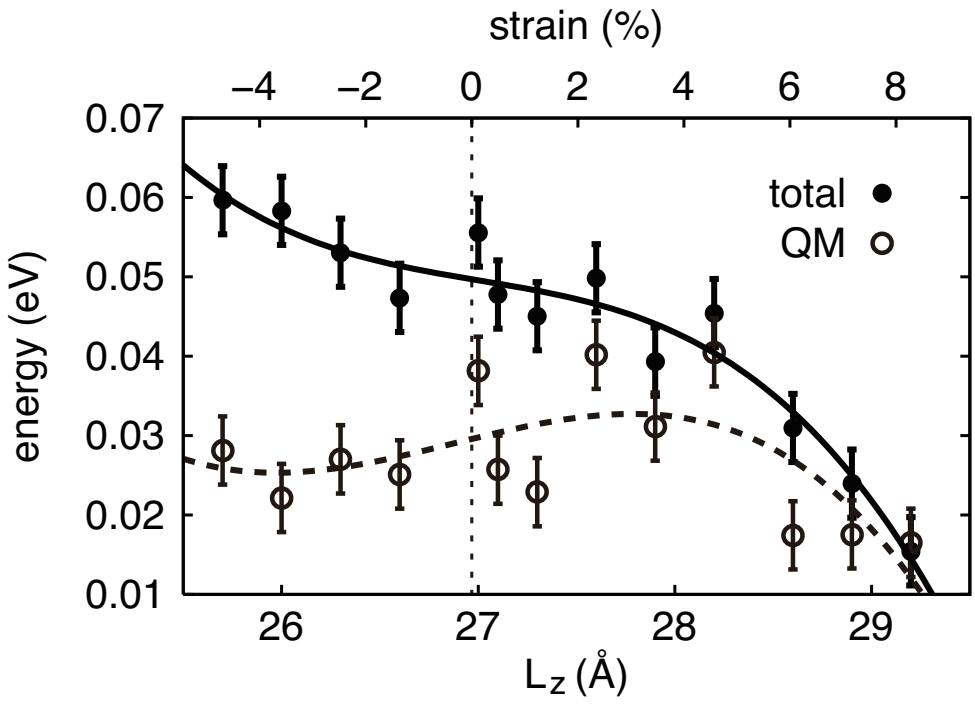

Figure 4.7: The activation energy for the hopping diffusion of the Li ion in the graphite at $T = 0$ K calculated using the hybrid QM-CL simulation method. The filled circles with the black curve represent the data evaluated using the total energy. The open circles with the gray curve represent the data using the energy of the QM region only. The strain corresponds to the variation of L_z from the equilibrium distance of 26.97 Å at 0 K. The error bars indicate the estimated overall errors relating to the convergence fluctuation in the real-space DFT method.

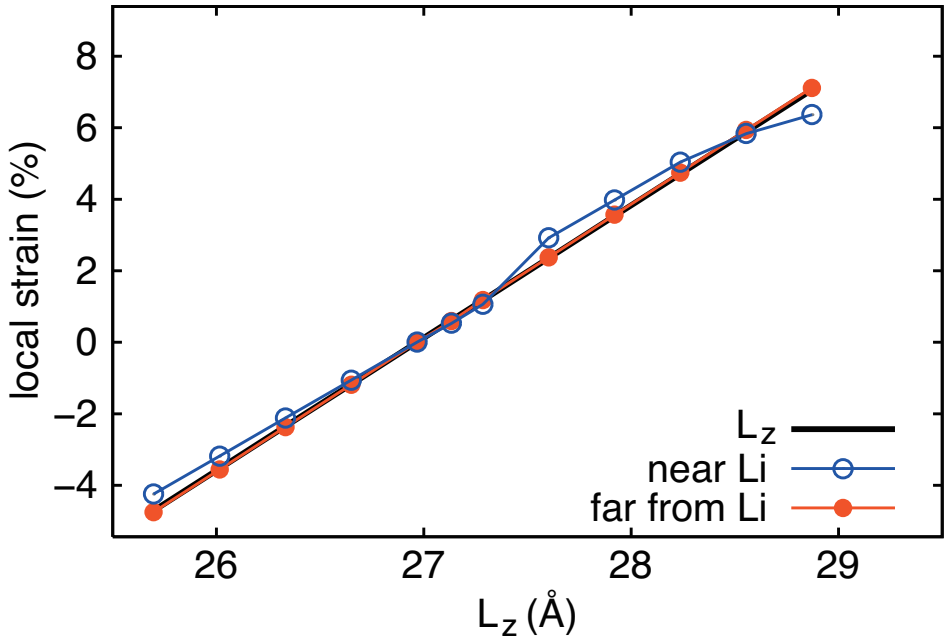

Figure 4.8: The local strains as functions of L_z calculated using the hybrid QM-CL simulation method at $T = 0$ K. The open blue spheres are for the region near the Li ion; the filled red spheres, for the region far from the Li ion. The black line represents the ideal case of uniform strain.

Table 4.1: The results of various quantities at the ground state (GS) and transition state (TS) calculated using the VASP code. The $E_{\rm ele}$, $E_{\rm vib}^{400\rm K}$, $S_{\rm vib}^{400\rm K}$, and $G^{400\rm K} = E_{\rm ele} + E_{\rm vib}^{400\rm K} + pV - TS_{\rm vib}^{400\rm K}$ are the electronic energy at $T = 0$ K, the vibrational energy including the zero-point energy, the phonon entropy, and the Gibbs free-energy at $T = 400$ K, respectively. The electronic energy is measured in reference to the standard states of the atomic elements.

	$E_{\rm ele}$ (eV)	pV (eV)	$E_{\rm vib}^{400\rm K}$ (eV)	$S_{\rm vib}^{400\rm K}$ (eV/K)	$G^{400\rm K}$ (eV)
GS	−7.94	2.79	13.88	0.0063	6.22
TS	−7.85	2.74	13.75	0.0059	6.26
Δ (TS-GS)	0.09	−0.06	−0.13	−0.00036	0.04

state that no substantial difference in the activation energy exists between the two results. In addition we calculate the activation free-energy using the phonon package MedeA [41]. Relatively large contribution of the phonon entropy $T\Delta S = -0.14$ eV is found at 400 K. Finally the difference in the Gibbs free-energy between the GS and TS becomes 0.04 eV.

It is known experimentally that the drastic lowering to one severalth of the Li diffusivity occurs in the Li-GIC at particular values of the Li density that correspond to the coexistence of different stage-structures [28]: random (dilute)-stage and stage-4, stage-4 and stage-3, etc. This has been thought to be attributed to the coexistence of two different phases and the movement of the phase boundary. From our findings about the stress-dependence of the Li diffusivity in the graphite explained above, we can propose another possible mechanism for the drastic lowering of the Li diffusivity as follows. Suppose a phase boundary in the Li-GIC in which one phase assumes the dilute random-stage and another does the stage-4, as illustrated in Fig. 4.9. The X-ray diffraction measurement showed that the averaged inter-layer distance gets longer as the stage structure advances relating to the increase in the Li density [42]. Therefore, due to the relative elongation of the averaged inter-layer distance in the stage-4 phase, compressive and stretching stresses work on average on the stage-4 and the random-stage sides, respectively, at the phase boundary (see, Fig. 4.9). We have demonstrated in Fig. 4.4 that only 2% compression in z-direction suppresses the Li diffusivity substantially:

the MSD in the -1.7% case is about one third of that in the 0.6% case. The compressive stress in the stage-4 side of the phase boundary may play a role to create a confining bank for the Li diffusion. If such a phase boundary extends to the entire system, significant lowering of the Li diffusivity should result.

Remarks on the proposed mechanism for the drastic lowering of the Li diffusivity at the stage-mixture situation are in order. (i) Though difference exists about the layer-stacking between the AA sequence around the Li-rich layers in the stage-4 structure and the AB sequence assumed in our simulation runs, we expect a similar suppression of the Li diffusivity due to compression occurs also in the stage-4 structure. (ii) Since the Li insertion expands the inter-layer distance by about 10%, the 2% compression of the averaged inter-layer distance that we just mentioned can be realized. (iii) Compressive stress also emerges in the random-stage side for the neighboring two layers with the Li ions inserted on the random-stage side and no Li ion on the stage-4 side, as illustrated in Fig. 4.9. However, because of the relatively low density of the Li ions in the random-stage structure as compared to the stage-4 structure, the Li ions in the random-stage structure should be affected little by such a compressive stress. Rather, the exclusive volume effect [43] that causes repulsive interaction between the Li ions located just above and below graphite layers should lower the Li diffusivity. In fact, the Li diffusivity decreases as the Li density increases in the random-stage [28]. (iv) In reality the graphite layers often warp and bend, which means the existence of mixture of the AA- and AB-sequences. Since the inter-layer distance is larger by 4% in the AA-sequence than in the AB-sequence, similar mechanism for the Li diffusivity may work also for this situation.

In all the simulation runs explained in the present paper, only a single Li-ion in the graphite is treated, in other words, mutual interaction between the Li ions is ignored. As already pointed out in Ref. [43] as the exclusive volume effect, the Li-Li interaction should affect the Li diffusivity. We are working on the issue by performing a larger scale hybrid QM-CL simulation, in which neighboring Li ions and their surrounding C atom are treated together as a single QM region. Such a large QM region is treated by our novel divide-and-conquer-type order-N DFT method to be reported in

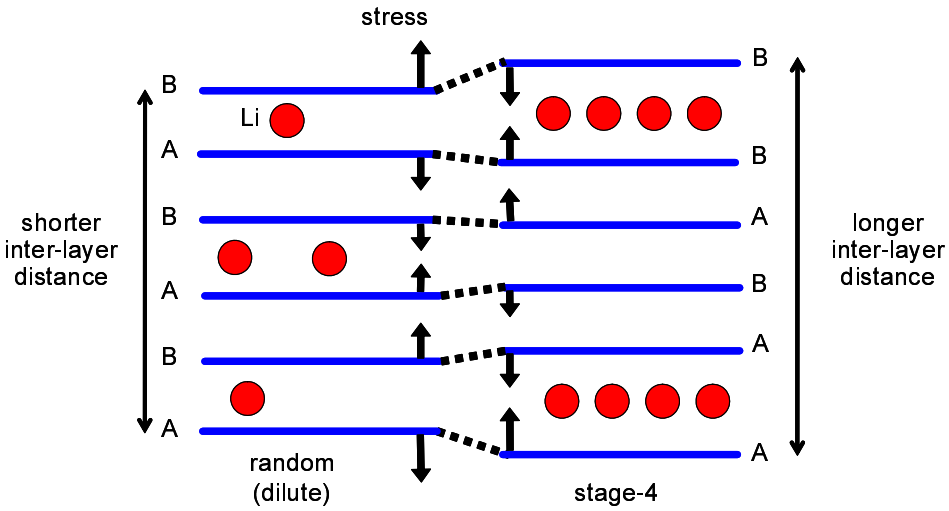

Figure 4.9: Schematic illustration of the phase boundary of the random-stage and stage-4 structures in the Li-GIC. The blue horizontal lines indicate the graphite layers. The stresses acting on the layers due the differences in the inter-layer distance, are depicted by the arrows.

a separate paper. Combined effects of the external stress and the Li-Li interaction will be clarified.

4.4 Conclusions

We have applied the hybrid QM-CL simulation code to analyze the stress dependence of the diffusivity of a single Li-ion in the graphite at $T = 423$ K by changing the averaged inter-layer distance (by plus and minus a few percent). The real-space DFT method has been applied to treat the QM region that is selected adaptively to include the Li and its surrounding C atoms. The weak C-C interaction (i.e., the dispersion force) acting between different C-layers has been modeled through the CL interatomic potential. Thereby we have found that the Li diffusivity is suppressed significantly in the compressed case, while no substantial change is observed in the stretched case. In the stretched case, the Li-ion motion has shown both hopping and ballistic modes. On the other hand, in the compressed case, the Li ion has diffused through the hopping mode only and has been found to be confined in a relatively small area at longer times; its mechanism has been explained in

terms of the cage effect. The activation energy for the hopping diffusion has been found as small as 0.1 eV at $T = 0$ K, in accordance with the fast thermal diffusion of the Li ion observed in the present simulation. From our findings about the stress-dependence of the Li diffusivity in the graphite, we have proposed a possible mechanism for the drastic lowering of the Li diffusivity at particular densities of Li observed experimentally in the Li-GIC.

Chapter 5

Enhanced thermal diffusion of Li in graphite by alternating vertical electric field

5.1 Introduction

Graphite can form various intercalation compounds by incorporating ions, atoms, and small molecules between the C layers. Among these, a lithium-graphite intercalation compound (Li-GIC) is put to practical use as a negative electrode of the Li-ion rechargeable battery[44]. In the battery, Li ions are shuttled between the positive and negative electrodes through a nonaqueous electrolyte and a separator in electrochemical reactions of discharging and recharging with the applied voltage. Such discharging and recharging reactions in the Li-ion battery involve the following key processes: the transport of Li ions in both electrode and electrolyte materials, the charge transfer at the electrolyte-electrode interfaces, and the internal structural changes of the electrodes as the Li density changes. There is much interest in advancing the power, capacity, recharging speed, and durability of the Li-ion battery relating to the recent electric power conservation and environmental problems. Among the key processes, the transport process of the Li ions in graphite is related directly to the recharging speed and power of the battery.

Lithium diffusivity in graphite has been investigated both experimentally and theoretically. The diffusion coefficients obtained in the experiments[28,

45] vary in a wide range of $10^{-5} \sim 10^{-12}$ cm^2/s depending on not only the experimental conditions but also the measurement methods. We here note that extracting the net diffusion coefficient of Li ions from measured data is not easy as it requires additional information on the inhomogeneous distribution of Li ions, the surface area of the sample, and other factors. On the other hand, Toyoura and coworkers [46, 47] evaluated by first-principles calculations the mean frequencies of the hopping of the Li ion in LiC_6 on the basis of the transition state theory; the hopping process involving interstitials and vacancies of graphite was considered. Persson *et al.* [48] calculated the Li diffusion coefficients of Li_xC_6 at $x > 0.2$ by kinetic Monte Carlo simulation using the Li migration barrier energy obtained by the first-principles method and the configurational energy of Li ions and vacancies evaluated with the cluster expansion method. They found that Li diffusivity depends principally on the inter-layer spacing at low Li densities and on the in-plane Li-Li interaction at high Li densities.

The Li ion in graphite creates a long-ranged stress field around itself by expanding the inter-layer spacing by about 10%. We have recently investigated the stress dependence of the diffusivity of the Li ion in graphite at a temperature $T = 423$ K using the hybrid quantum (QM)-classical (CL) simulation method by changing the average inter-layer spacing [49]. In the method, a relatively small region for the density-functional theory of electrons selected adaptively around the Li ion was embedded in the total system described by classical interatomic potentials, to include the effect of the surrounding C atoms in the QM region at a reasonable computational cost (see the following paragraphs for details). The layers in graphite were assumed to form an AB stacking sequence as we were interested in a low-Li-density situation. Our findings obtained include the following [49]: (i) The majority of the valence electrons of the Li atom is transferred to the surrounding C atoms irrespective of the average inter-layer spacing, resulting in the Li ion state. (ii) In the few %-stretched and equilibrium cases, the Li ion migrates in the inter-layer spacing with changes between the hopping and ballistic modes. In the hopping mode, the Li ion shows frequent transitions between the upper and lower vertical sites in the spacing that are located near the upper and lower layers, respectively. The two vertical sites emerge

because the Li ion is stable at the location above or below the center of a six-membered C ring by less than half of the inter-layer distance in thermally expanded graphite with an AB stacking sequence [see Fig. 5.1 (top)]. Ballistic motion can occur when the instantaneous inter-layer spacing around the Li ion becomes larger than 3.85 Å. (iii) In the few %-compressed case, the Li ion diffuses in the hopping mode only. This shows the tendency of confinement due to deformed layers (i.e., the cage effect). Considering these, in this paper, we will firstly analyze the relation between the vertical transition and diffusivity of the Li ion in graphite. Motivated by the results of the present analyses, we will secondary perform a series of hybrid QM-CL simulation runs to demonstrate an enhanced thermal diffusivity of Li ions by applying alternating electric fields perpendicular to the layers.

5.2 Settings in simulation

The simulation system in the present and former studies is composed of $3,072$ C atoms and a single Li atom, whose positions are $\{\boldsymbol{R}_I\}$, at temperature $T =$ 423 K under the periodic boundary conditions (PBCs) as shown in Fig. 5.1. Eight layers form the AB stacking sequence in the vertical (z) direction. The system dimensions are $(L_x, L_y, L_z) = (34.44 \text{ Å}, 29.83 \text{ Å}, 28.55 \text{ Å})$. Here, L_x and L_y are the equilibrium values at $T = 0$ K obtained in the hybrid QM-CL simulation, while L_z corresponds to a 2.9% expansion of the equilibrium value at $T = 0$ K to take into account thermal expansion. A cluster of atoms composed of the Li and surrounding C atoms in the neighboring layers that sandwich the Li ion is reselected as the QM region with an interval of about 50 fs or longer depending on the situation; the rest of the whole system is called the CL region. Various electric fields in the z-direction are applied to the system in this study, while L_z was varied in the former study.

We advance the hybrid QM-CL simulation method to investigate Li dynamics in graphite at high accuracies with both effects of all the C atoms in the system and external electric field included. The buffered cluster method[3] is used to realize a seamless mechanical coupling of the QM and CL regions at the atomic scale. Since the electronic structure calculation is performed for the QM region only, the higher accuracy in the electrochemical

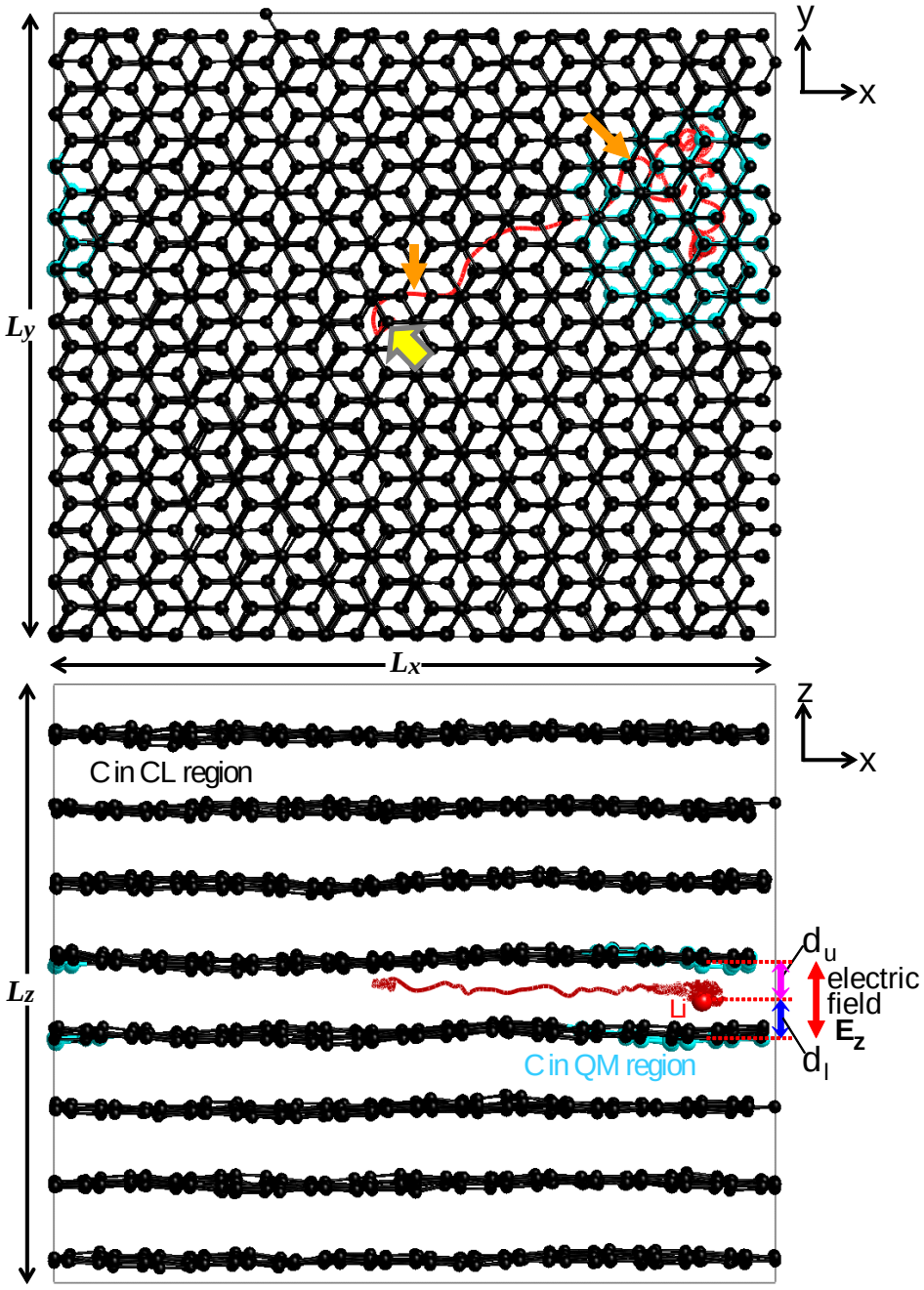

Figure 5.1: Top (x-y) and side (x-z) views of simulation system in hybrid QM-CL simulation run at $T = 423$ K with zero external electric field. The large and medium spheres are respectively the Li and C atoms in the QM region. The small spheres with bonds are C atoms in the CL region. The curve is the trajectory of the Li ion for the 10 ps obtained in the simulation run. The large arrow depicts the initial position of the Li ion. The small arrows indicate the places where the changes between the hopping and ballistic modes occur during the migration. The C-Li distances d_{u} and d_{l} are depicted.

reaction is expected for the larger QM region. For fast computation, the dynamic reselection[32] of C atoms around the Li ion in motion follows the rule to reselect about 60 C atoms in units of six-membered C rings from the instantaneous atomic configuration. In the method, we introduce buffer atoms for the QM calculation of the QM region. The species of the buffer atoms in the present setting is H, whose positions are determined at every time step to minimize the potential energy of a corresponding classical atomic cluster. The atomic forces during Li diffusion are confirmed to have sufficient accuracies in separate simulation runs. Assuming the inactiveness of C atoms in the CL region to the external electric field, we apply uniform electric fields in the z-direction to the QM region with various amplitudes and frequencies to see their possible effects on the Li diffusivity. The velocity-Verlet algorithm is used to integrate Newton's equations of motion of all the atoms using the atomic forces calculated. The velocity scaling with a factor common to all the atoms is also applied to maintain the system temperature.

For the QM region with buffer atoms under the external electric field $\boldsymbol{E}$, we consider the following Kohn-Sham (KS) equation in the DFT:

$$\left[-\frac{\nabla^2}{2} + v_{\rm eff}(\boldsymbol{r}, \{\boldsymbol{R}_I\}) + \boldsymbol{E}\cdot\boldsymbol{r}\right]\psi_i(\boldsymbol{r}) = \varepsilon_i\psi_i(\boldsymbol{r}) \tag{5.1}$$

with an eigen orbital and energy of ψ_i and ε_i, respectively (the atomic unit is used). Here, $v_{\rm eff}(\boldsymbol{r}, \{\boldsymbol{R}_I\})$ is the effective potential energy for an electron at $\boldsymbol{r}$ without the external electric field. Charge neutrality is assumed in the calculation. The force on atom-I is obtained by adding $\boldsymbol{F}_I = Z_I\boldsymbol{E}$ (Z_I is the ion charge) to the atomic force caused by electron-electron, electron-ion, and ion-ion interactions. We use the real-space implemented density-functional theory (DFT) code by representing the KS orbitals and Hartree field on the uniform Cartesian mesh points. The fourth-order finite-difference method is used for the Laplacian operation [36]. The multigrid method [37] is employed to accelerate convergence. For parallel computation, those data on the mesh points are decomposed into computation nodes of a parallel machine for storing and computation. The mesh size $h = 0.45$ $a_{\rm B}$ (1 $a_{\rm B} \approx 0.5292$ Å), which corresponds to the cutoff energy $(\pi/h)^2 \approx 49$ Ry (1 Ry ≈ 13.6 eV) in the planewave-based DFT method. In addition, the smaller mesh size of $h/3$ is used only around the atoms. The real-space DFT method has

the advantage of applicability to various settings of the external electric field. The norm-conserving pseudopotentials [34] are used to describe the interaction of valence electrons and ions. The generalized gradient approximation formula [35] is adopted for the exchange-correlation energy. Details of the QM calculation algorithm were described in refs. [31, 15, 33].

The classical interatomic potential by Brenner[16] is applied to C atoms in the CL region. We employ the parameter values listed in Table I in ref. [16], except for the equilibrium distance. The equilibrium distance is set to 1.33116 Å so that the equilibrium lattice constant of graphite matches well with that obtained in the QM region, which is slightly longer than that assumed in ref. [16]. Such an adjustment of parameters in the CL potential is necessary in order not to create artificial stress at the QM-CL boundary in the hybrid QM-CL simulation method [18]. In the Brenner-type potential, only the interaction between nearest-neighbor atoms in the same layer is considered. To take into account the inter-layer interaction due to dispersion (or the van der Waals) forces, we add the following interatomic potential particularly for C atoms in different layers:

$$V_{\mathrm{vdW}}(R) = 4\varepsilon \left\{ \left(\frac{\sigma}{R}\right)^{12} - g(Z) \left(\frac{\sigma}{R}\right)^{6} \right\} f(R), \tag{5.2}$$

with the distance R between C atoms. The basic form of $V_{\mathrm{vdW}}(R)$ is that of the Lennard-Jones potential. The function $f(R)$ works to cutoff the potential gradually at a long distance of approximately 5.6 Å. The coordination-number-dependent function $g(Z)$, which takes on values between 0 and 1, is a measure of the degree of similarity to the AA stacking sequence of neighboring layers using the coordination number Z of the C atoms in a neighboring layer for a given atom. The parameters $\varepsilon = 2.84$ meV and $\sigma = 3.35$ Å are determined to reproduce the experimental inter-layer energy and spacing, respectively. With the classical interatomic potential thus constructed, the elastic constant of pure graphite for the vertical direction in the AB stacking sequence becomes $c_{33} = 34.5$ GPa , which is in good agreement with the experimental value of 36.5 GPa [26].

5.3 Results and discussion

Firstly, we analyze the relation between the vertical position and diffusion behavior of the Li ion observed in the hybrid simulation run with a zero electric field, i.e., $\boldsymbol{E} = 0$. As seen in Fig. 5.1, the Li ion diffuses in the inter-layer spacing with transitions in the vertical position. Figure 5.2 (middle) shows the time evolutions of the distances $d_{\rm u}$ and $d_{\rm l}$ between the Li ion and the center-of-mass positions of QM-region C atoms in the upper and lower layers, respectively. The time evolutions of absolute values of Li displacement in the x-, y-, and z-directions $|(\boldsymbol{R}_{\rm Li}(t) - \boldsymbol{R}_{\rm Li}(0))_{x,y,z}|$ are shown in Fig. 5.2 (bottom). In most of the period of $t = 0$ to 1 ps, $d_{\rm l}$ is shorter than $d_{\rm u}$, which means that the Li ion is trapped near the lower layer. During the period, the Li ion hardly diffuses, as shown in Fig. 5.2 (bottom). In the following period of $t = 1.0$ to 1.2 ps, on the other hand, $d_{\rm l}$ and $d_{\rm u}$ are nearly equal and the Li diffusivity is relatedly high. Such a relation between $d_{\rm l}, d_{\rm u}$, and the in-plane displacements of the Li ion can also be seen at approximately $t = 1.6$ ps and 4.2 ps in Fig. 5.2. We may state that Li diffusivity is enhanced when the Li ion escapes from one of the two stable vertical sites to move around the middle of the upper and lower layers where a resisting force on the Li ion for the perpendicular (x or y) motion is relatively weak.

Motivated by the finding stated above, we think of increasing the mean probability of the Li residence around the middle of the upper and lower layers to enhance the diffusivity of the Li ion in graphite by applying an alternating vertical electric field. Figure 5.3 shows the mean squared displacements of the Li ion as functions of time $\langle|(\boldsymbol{R}_{\rm Li}(t) - \boldsymbol{R}_{\rm Li}(0))|^2\rangle$ obtained in the hybrid QM-CL simulation runs at $T = 423$ K with electric field amplitudes $E_z^{\rm amp} =$ 0.0, 0.14, and 0.43 V/Å and frequencies $f = 0.4$, 0.8, and 1.7 THz. For better statistics, the time origins are set every 10 fs in a simulation run with a total of 5 ps. Since the mean squared displacements of the Li ion for $t = 0 \sim 2$ ps have small statistical errors to some extent, we can see the following qualitative characteristics to depend on the electric field. As $E_z^{\rm amp}$ increases with $f = 0.4$ THz, the Li diffusivity gets lower. This is because the Li ion experiences a force to stay around one of the two stable vertical sites exerted by the vertical electric fields at such a relatively low frequency. The

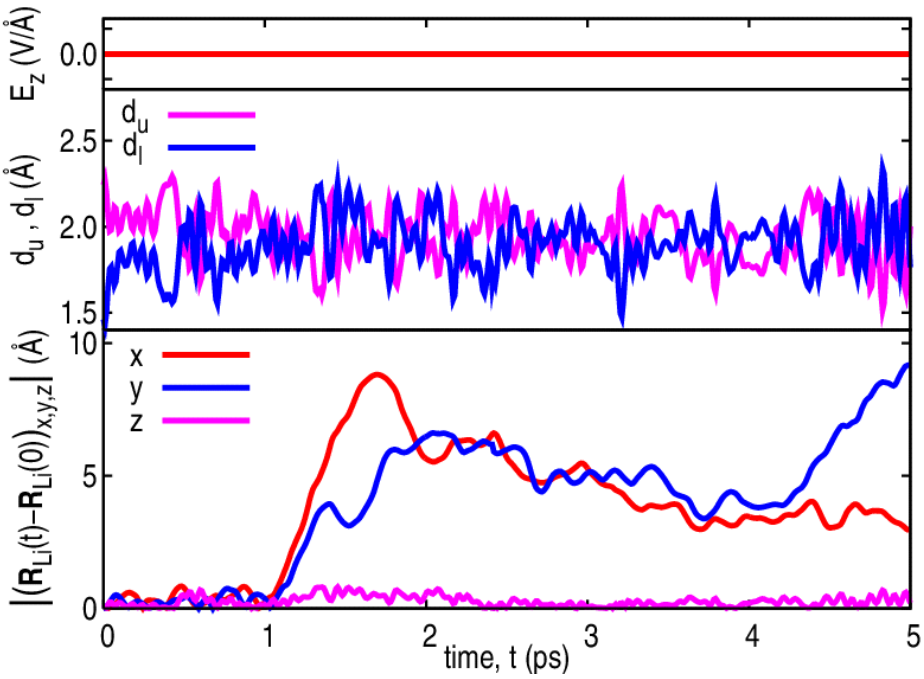

Figure 5.2: Diffusion behavior of Li ion in graphite at $T = 423$ K with zero external electric field, observed in hybrid QM-CL simulation run. The time evolutions of the external electric field, d_{u} and d_{l}, and the absolute values of the Li displacements in three directions are depicted in top, middle, and bottom panels, respectively.

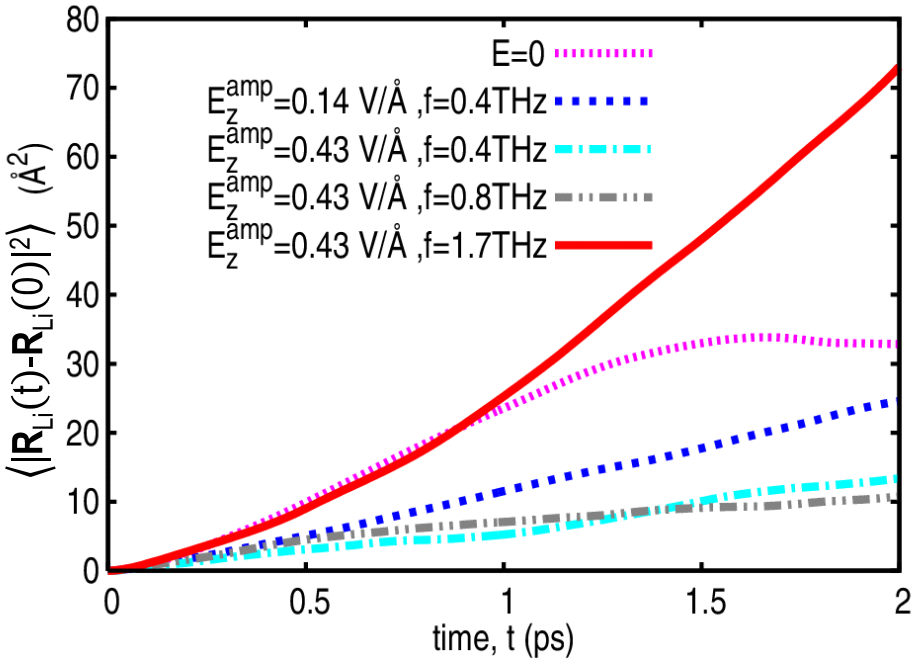

Figure 5.3: Time evolutions of mean squared displacements of Li ion obtained in hybrid QM-CL simulation runs at $T = 423$ K with various external electric fields. For better statistics, the time origins are set every 10 fs in a total simulation period of 5 ps.

activation energy for the hopping diffusion of the Li ion is estimated [49] as about 0.04 eV for the present system size $L_z = 28.55$ Å. Since the vertical distance between the stable vertical site and the transition state site is about 0.2 Å, $E_z^{\mathrm{amp,thres}} = 0.04/0.2 = 0.2$ V/Å may be the threshold value for such a vertical transition of the Li ion to occur without the thermal energy. The Li ion is expected to escape quickly from one of the two stable vertical sites following the time evolution of the electric field if $E_z^{\mathrm{amp}} > E_z^{\mathrm{amp,thres}}$.

We therefore analyze the f dependence of $\langle|(\boldsymbol{R}_{\mathrm{Li}}(t) - \boldsymbol{R}_{\mathrm{Li}}(0))|^2\rangle$ for $E_z^{\mathrm{amp}} = 0.43$ V/Å, which is larger than $E_z^{\mathrm{amp,thres}}$. As shown in Fig. 5.3, the Li diffusivity at $f = 0.8$ THz is similar to that at $f = 0.4$ THz and that the Li diffusivity at $f = 1.7$ THz is remarkably high. The time evolutions of the Li-C distances d_{u} and d_{l} for $E_z^{\mathrm{amp}} = 0.43$ V/Å at $f = \{0.4\ \mathrm{THz}, 1.7\ \mathrm{THz}\}$ are shown in Fig. 5.4. At $f = 0.4$ THz, the vertical position of the Li ion is high (low) when the electric field directs upward (downward) as seen in

Fig. 5.4(a). Since the Li ion hardly diffuses when it stays at one of the two stable vertical sites, the effective diffusivity becomes low at such a low frequency. At a high frequency of $f = 1.7$ THz, the Li ion changes its vertical position in a chaotic manner with the large and alternating vertical forces on it owing to the external electric field, as shown in Fig. 5.4(b). It appears that the vertical motion of the Li ion cannot catch up with such a fast change in the direction of the external electric field. In other words, the Li ion experiences a retarding force from the external electric field before arriving at a stable vertical site. The Li ion therefore increases its probability of residing around the middle of the upper and lower layers, resulting in a significant enhancement of Li diffusivity. We here mention about the electron density obtained in the QM calculation with the electric field applied. Even for the largest amplitude $E_z^{\rm amp} = 0.43$ V/Å, the electrons are found to reside around the C atoms and the atomic forces calculated satisfy well the action-reaction law.

No experimental report exists about the vibrational frequency peak of Li-GIC in the range of $1 \sim 2$ THz. For graphite, the low-frequency mode of $E_{2g(1)}$ is observed at 1.26 THz in the Raman measurement [25]. If the oscillation frequency of the external electric field is tuned to the mode, it is likely that the vertical vibration of the layers in graphite enhances Li diffusivity further by increasing the probability of the Li residence around the middle of the upper and lower layers. We note that no such vibration of the layers is observed in the present simulation runs. Technologies for generating high-intensity radiation in the terahertz range have been advancing rapidly in recent years, for example, using the gyrotron system [50] and the coherent transition radiation from a linear accelerator whose field amplitude reaches over 0.2 V/Å [51]. Experiments to demonstrate our present prediction of enhanced Li diffusivity in graphite by using an alternating vertical electric field should be possible in the near future.

5.4 Conclusions

In summary, we have developed a hybrid QM-CL simulation code to analyze the effects of the external electric field on the Li diffusivity in graphite. The

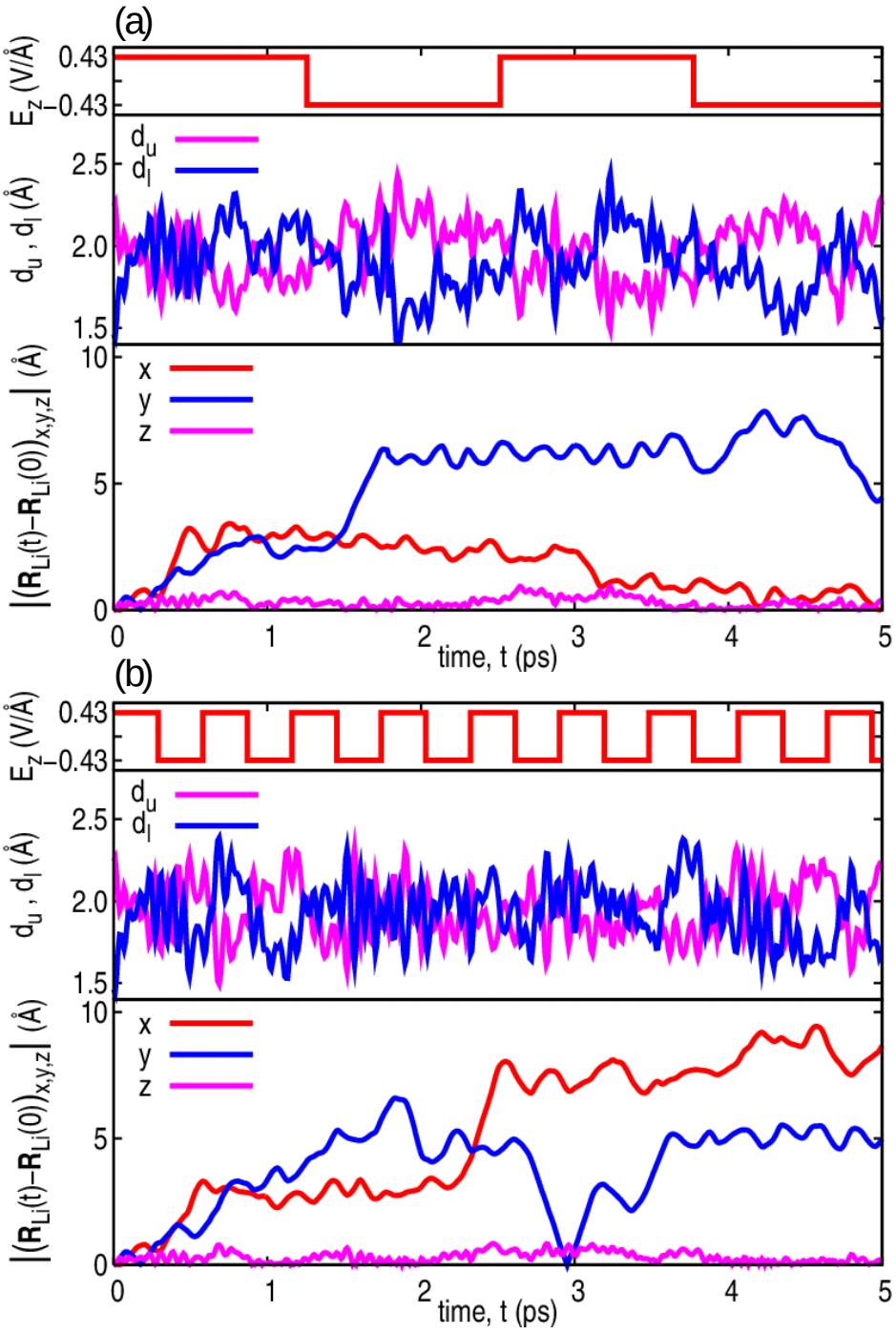

Figure 5.4: Same as Fig. 5.2, but with the external electric field amplitude $E_z^{\text{amp}} = 0.43$ V/Å. (a) At frequency $f = 0.4$ THz. (b) At $f = 1.7$ THz.

real-space DFT method has been used to treat the QM region under the external electric field selected adaptively to include the Li and its surrounding C atoms. The dispersion force acting between the C atoms in different layers has been modeled to be included in the classical interatomic potential. We have found that the in-plane diffusivity of the Li ion at $T = 423$ K is enhanced significantly by the electric field perpendicular to the C-layers if the amplitude $E_z^{\rm amp} > 0.2$ V/Å and the frequency f is as high as 1.7 THz. The mechanisms of the enhanced diffusivity have been explained in terms of the increased probability of the Li residence around the middle of the upper and lower layers, resulting in a weak interaction between the Li ion and the graphite layer.

In this study, we have considered the system containing a single Li ion in the graphite. As already pointed out in ref. [48], the Li-Li interaction should affect Li diffusivity in Li-GIC at a higher concentration of Li. We are working on the issue by performing a larger-scale hybrid QM-CL simulation of Li diffusivity in graphite, in which neighboring Li ions and their surrounding C atom are treated together as a single QM region. Such a large QM region is treated by the divide-and-conquer-type real-space DFT method [52] developed recently. The combined effects of the long-range stress field, external electric field, and Li-Li interaction will be clarified in the future.

Chapter 6

Summary

In this thesis, we have studied on the Li diffusivity in the Li-GIC under both stress and external electric field. In order to describe combined effects of the electronic structure and mechanical stress at a realistic setting for the dynamics, we have developed the hybrid QM-CL simulation code in which the QM region described with the DFT is embedded in the CL system. The real-space DFT code implemented using the finite difference method has been adopted to treat the QM region that is selected adaptively to include the Li and its surrounding C atoms in the Li-GIC. On the other hand, the classical MD method using empirical interatomic potential has been applied to the movement of the rest C atoms. The Brenner-type potential has been used for the intra-layer interatomic potential between C atoms. Novel inter-layer interaction model acting between the C atoms in different C-layers has been constructed. Although the weak dispersion force for the inter-layer interaction of the graphite cannot be taken into consideration in the conventional DFT method, it can be incorporated easily through the CL interatomic potential model in the hybrid QM-CL method. The validity of both potential models for this study has been confirmed by the separate calculation of the diamond and graphite prior to the hybrid simulation. Buffered cluster method is applicable to couple the QM and CL regions.

Let us summarize the results obtained from our hybrid QM-CL simulations of the Li-GIC as follow:

(I) In preparatory calculations in the hybrid QM-CL simulation for the

Li-GIC, we have set the QM regions in various shapes and sizes to find that the crystalline structure is sufficiently stable with no unreasonable distortion at the QM-CL boundary. The hybrid QM-CL simulation adopted in this study shows good conservation of the total energy of the QM-CL hybrid system during the simulation run. The charge density at a dangling bond of a buffer atom localizes well with little influence on the electronic structure in the central area of the QM region.

(II) Since the valence electron density around the Li atom becomes almost zero, the Li has positive charge and the C atoms of graphite have negative charge as the result of charge transfer from Li to C atoms. The diffusion coefficient calculated by the mean-square-displacement of Li ion in the present hybrid dynamics has been estimated as 7×10^{-5} cm^2/sec, which is in good agreement with the experimental one. We have confirmed that the Li-GIC changes into AA-type stacking structure as the Li density becomes higher and that the Li ion moves well when the stacking changes from AA to AB sequence.

(III) We have applied the hybrid QM-CL simulation code to analyze the stress dependence of the diffusivity of Li in the graphite. Simulation runs have been performed at temperature of $T = 423$ K, and various stress fields have been created by changing the averaged inter-layer distance (by plus and minus a few percent). We have found that the Li diffusivity is suppressed significantly in the compressed case, while no substantial change is observed in the stretched case. In the stretched case, the Li-ion motion has shown both hopping and ballistic modes. On the other hand, in the compressed case, the Li ion has diffused through the hopping mode only and has been found to be confined in a relatively small area at longer times; its mechanism has been explained in terms of the cage effect. The activation energy for the hopping diffusion has been found as small as 0.1 eV at $T = 0$ K, in accordance with the fast thermal diffusion of the Li ion observed in the present simulation.

(IV) The abruptly lowering of the diffusion coefficient of Li at the

coexistence of different stage-structures was observed experimentally in the Li-GIC. This has been thought to be attributed to the coexistence of two different phases. In addition, we think that our findings about the stress-dependence of the Li diffusivity in the graphite may be another possible mechanism for the feature of the Li diffusivity mentioned above.

(V) We have analyzed the relation between the vertical position and diffusivity of the Li ion in graphite. The Li diffusivity is enhanced when the Li ion escapes from one of the two stable vertical sites to move around the middle of the upper and lower C-layers where a resisting force on the Li ion for the perpendicular motion is relatively weak.

(VI) The effects of the external electric field on the Li diffusivity in graphite have been analyzed. We have thereby found that the in-plane diffusivity of the Li ion at $T = 423$ K is enhanced significantly by the electric field perpendicular to the C-layers if the amplitude $E_z^{\rm amp} > 0.2$ V/Å and the frequency is as high as 1.7 THz. Mechanisms of the enhanced diffusivity have been explained in terms of the increased probability of the Li residence around the middle of the upper and lower layers, resulting in weak interaction between the Li ion and the graphite layer.

Present simulation has focused on the system containing only a single Li-ion in the graphite. In reality, plural Li atoms exist in the Li-GIC and the Li-Li interaction should affect the Li diffusivity. We are now working on the issue by performing a larger scale hybrid QM-CL simulation of the Li diffusivity in graphite, in which neighboring Li ions and their surrounding C atoms will be treated together as a single QM region. Such a large QM region is treated by the divide-and-conquer-type real-space DFT method developed recently by us. Combined effects of the long-ranged stress field, external electric field, and the Li-Li interaction will thereby be clarified.

In the Li-ion battery, the Li ions are intercalated into graphite electrodes from nonaqueous electrolytes by the applied voltage (i.e. external electric field). Moreover, it is well known that electrochemical reactions involving the decomposition of the electrolyte occur on the interface of negative electrode

and nonaqueous electrolyte in addition to Li intercalation. The solid products formed by the decomposition of nonaqueous electrolytes deposit on the graphite surface, which form the so-called the solid electrolyte interphase (SEI) layer. We will challenge to perform the hybrid simulation to reveal such microscopic details of chemical reactions and dynamics in complicated nano-structures.

Acknowledgments

First and foremost, I would like to thank my supervisor, Professor Suji Ogata, for his guidance throughout my studies. I am grateful to Professor Toshiyuki Gotoh, Professor Masaru Sugiyama and Professor Akira Takahashi for their valuable comments at the critical stage of my thesis.

I wish to thank Dr. R. Kobayashi, Dr. T. Tamura and the members of Ogata Laboratory in Nagoya Institute of Technology for helpful discussions. I also thank Dr. R. Asahi and other members of Materials Design Laboratory in Toyota Central R&D Labs., Inc. for their constructive comments and suggestions of my work.

I would like to thank Professor S. Hyodo (University of Hyogo) who provided me the opportunity to start this study.

Finally, I thank my husband for his constant support and encouragement.

References

[1] C. Julien and J. Pereira-Ramos: *New trends in intercalation compounds for energy storage* (Springer Netherlands, 2002), Vol. 61.

[2] S. Dapprich, I. Komáromi, K. Byun, K. Morokuma, and M. Frisch: Journal of Molecular Structure: THEOCHEM **461** (1999) 1.

[3] S. Ogata: Phys. Rev. B **72** (2005) 045348.

[4] W. Kohn, L. Sham, et al.: Phys. Rev **140** (1965) A1133.

[5] M. C. Payne, M. P. Teter, D. C. Allan, T. A. Arias, and J. D. Joannopoulos: Rev. Mod. Phys. **64** (1992) 1045.

[6] G. Kresse and J. Furthmüller: Phys. Rev. B **54** (1996) 11169.

[7] D. M. Bylander, L. Kleinman, and S. Lee: Phys. Rev. B **42** (1990) 1394.

[8] L. Kleinman and D. M. Bylander: Phys. Rev. Lett. **48** (1982) 1425.

[9] J. P. Perdew and A. Zunger: Phys. Rev. B **23** (1981) 5048.

[10] e.g., W. H. Press, S. A. Teukolsky, W. T. Vetterling, and B. P. Flannery: *Numerical Recipies in Fortran 77, 2nd Ed.* (Cambridge Univ Press, New York, 1992).

[11] J. R. Chelikowsky, N. Troullier, and Y. Saad: Phys. Rev. Lett. **72** (1994) 1240.

[12] U. Waghmare, H. Kim, I. Park, N. Modine, P. Maragakis, and E. Kaxiras: Comput. Phys. Commun. **137** (2001) 341 .

[13] J. Iwata, D. Takahashi, A. Oshiyama, T. Boku, K. Shiraishi, S. Okada, and K. Yabana: J. Comput. Phys. **229** (2010) 2339.

[14] T. Ono and K. Hirose: Phys. Rev. Lett. **82** (1999) 5016.

[15] S. Ogata, F. Shimojo, R. Kalia, A. Nakano, and P. Vashishta: Comput. Phys. Commun. **149** (2002) 30.

[16] D. Brenner: Phys. Rev. B **42** (1990) 9458 [Errata **46** (1992) 1948].

[17] J. Tersoff: Phys. Rev. B **39** (1989) 5566.

[18] T. Kouno and S. Ogata: J. Phys. Soc. Jpn. **77** (2008) 054708.

[19] P. Erhart and K. Albe: Phys. Rev. B **71** (2005) 035211.

[20] *Numerical data and functional relationships in science and technology*, ed. H. Ullmaier, Landolt–Börnstein New Series, Group III, Vol. 29, Pt. A, (Springer, Heidelberg, 1991).

[21] Y. Baskin and L. Meyer: Phys. Rev. **100** (1955) 544.

[22] L. Benedict, N. Chopra, M. Cohen, A. Zettl, S. Louie, and V. Crespi: Chemical physics letters **286** (1998) 490.

[23] R. Zacharia, H. Ulbricht, and T. Hertel: Phys. Rev. B **69** (2004) 155406.

[24] M. Kato, N. Narita, and S. Suzuki: Report of Research Institute of Industrial Technology A, Nihon University (in Japanese) **39** (2006) 61.

[25] R. Kostić, M. Mirić, T. Radić, M. Radović, R. Gajić, and Z. V. Popović: Acta Phys. Pol. A **116** (2009) 718.

[26] O. L. Blakslee, D. G. Proctor, E. J. Seldin, G. B. Spence, and T. Weng: J. Appl. Phys. **41** (1970) 3373.

[27] Eizi and Hirota: J. Mol. Spectrosc. **77** (1979) 213 .

[28] A. Funabiki, M. Inaba, Z. Ogumi, S. Yuasa, J. Otsuji, and A. Tasaka: J. Electrochem. Soc. **145** (1998) 172.

[29] K. Kganyago and P. Ngoepe: Phys. Rev. B **68** (2003) 205111.

[30] T. Ohzuku, Y. Iwakoshi, and K. Sawai: J. Electrochem. Soc. **140** (1993) 2490.

[31] S. Ogata, E. Lidorikis, F. Shimojo, A. Nakano, P. Vashishta, and R. Kalia: Computer Physics Communications **138** (2001) 143.

[32] S. Ogata, Y. Abe, N. Ohba, and R. Kobayashi: J. Appl. Phys. **108** (2010) 064313.

[33] F. Shimojo, T. J. Campbell, R. K. Kalia, A. Nakano, P. Vashishta, S. Ogata, and K. Tsuruta: Future Gener. Comp. Syst. **17** (2000) 279 .

[34] N. Troullier and J. L. Martins: Phys. Rev. B **43** (1991) 1993.

[35] J. P. Perdew, K. Burke, and M. Ernzerhof: Phys. Rev. Lett. **77** (1996) 3865.

[36] J. R. Chelikowsky, N. Troullier, and Y. Saad: Phys. Rev. Lett. **72** (1994) 1240.

[37] A. Brandt: Math. Comput. **31** (1977) 333.

[38] J. Nelson and D. Riley: P. Phys. Soc. **57** (1945) 477.

[39] Y. Qi, H. Guo, J. Louis G. Hector, and A. Timmons: J. Electrochem. Soc. **157** (2010) A558.

[40] G. Kresse and J. Furthmüller: Phys. Rev. B **54** (1996) 11169.

[41] MedeA-Phonon, Materials Design, Inc., 2003, based on K. Parlinski, Phonon 3.11: (2002).

[42] N. Takami, A. Satoh, M. Hara, and T. Ohsaki: J. Electrochem. Soc. **142** (1995) 371.

[43] S. A. Safran and D. R. Hamann: Phys. Rev. Lett. **42** (1979) 1410.

[44] R. Yazami and P. Touzain: J. Power Sources **9** (1983) 365 .

[45] H. Yang, H. Bang, and J. Prakash: J. Electrochem. Soc. **151** (2004) A1247.

[46] K. Toyoura, Y. Koyama, A. Kuwabara, F. Oba, and I. Tanaka: Phys. Rev. B **78** (2008) 214303.

[47] K. Toyoura, Y. Koyama, A. Kuwabara, and I. Tanaka: J. Phys. Chem. C **114** (2010) 2375.

[48] K. Persson, Y. Hinuma, Y. Meng, A. Van der Ven, and G. Ceder: Phys. Rev. B **82** (2010) 125416.

[49] N. Ohba, S. Ogata, T. Tamura, S. Yamakawa, and R. Asahi: CMES-Comp. Model. Eng. **75** (2011) 247.

[50] T. Saito, T. Notake, Y. Tatematsu, A. Fujii, S. Ogasawara, L. Agusu, T. Idehara, S. Kubo, T. Shimozuma, K. Tanaka, M. Nishiura, K. Kawahata, and V. N. Manuilov: J. Phys. Conf. Ser. **227** (2010) 012013.

[51] D. Daranciang, J. Goodfellow, M. Fuchs, H. Wen, S. Ghimire, D. A. Reis, H. Loos, A. S. Fisher, and A. M. Lindenberg: Appl. Phys. Lett. **99** (2011) 141117.

[52] N. Ohba, S. Ogata, T. Kouno, T. Tamura, and R. Kobayashi: submitted to Comput. Phys. Commun.